UC San Diego

UC San Diego Electronic Theses and Dissertations

Title

Conductive polymers improve human stem cell-derived cardiomyocyte function in two-dimensional and three-dimensional cultures

Permalink

https://escholarship.org/uc/item/9890v3bd

Author

Gonzalez, Gisselle

Publication Date

2024

Supplemental Material

https://escholarship.org/uc/item/9890v3bd#supplemental

Peer reviewed|Thesis/dissertation

eScholarship.org Powered by the California Digital Library
University of California

UNIVERSITY OF CALIFORNIA SAN DIEGO

Conductive polymers improve human stem cell-derived cardiomyocyte function in two-dimensional and three-dimensional cultures

A Dissertation submitted in partial satisfaction of the requirements
for the degree Doctor of Philosophy

in

Bioengineering

by

Gisselle Gonzalez

Committee in charge:

Professor Adam J. Engler, Chair
Professor Brian Aguado
Professor Shaochen Chen
Professor Shadi A. Dayeh

2024

Copyright

Gisselle Gonzalez, 2024

All rights reserved.

The Dissertation of Gisselle Gonzalez is approved, and it is acceptable in quality and form for publication on microfilm and electronically.

University of California San Diego

2024

DEDICATION

Para mis padres, que sacrificaron tanto por mí.

TABLE OF CONTENTS

DISSERTATION APPROVAL PAGE iii

DEDICATION iv

TABLE OF CONTENTS v

LIST OF FIGURES vii

LIST OF TABLES viii

LIST OF SUPPLEMENTAL FILES ix

ACKNOWLEDGEMENTS x

VITA xiii

ABSTRACT OF THE DISSERTATION xiv

Chapter 1 Engineering the niche to differentiate and deploy cardiovascular cells 1

1.1 Abstract 1

1.2 Introduction 1

1.3 Results 2

1.4 Conclusion 9

1.5 Figures 10

1.6 Acknowledgements 11

Chapter 2 Conductive electrospun polymer improves stem cell-derived cardiomyocyte function and maturation 12

2.1 Abstract 12

2.2 Introduction 13

2.3 Materials and methods 14

2.4 Results and discussion 23

2.5 Conclusion 29

2.6 Figures 31

2.7 Supplemental figures 37

2.8 Acknowledgements 39

Chapter 3 Conductive microfibers improve stem cell-derived cardiac spheroid maturation 40

3.1 Abstract.....40

3.2 Introduction 41

3.3 Materials and methods.....42

3.4 Results and discussion.....47

3.5 Conclusion.....53

3.6 Figures 55

3.7 Tables 60

3.8 Supplemental figures.....61

3.9 Acknowledgements 63

REFERENCES 64

LIST OF FIGURES

Figure 1.1: *In vitro* differentiation methods and their comparison to *in vivo* cardiac tissues..... 10

Figure 1.2: Engineered cues presented to hPSC-derived myocytes. 11

Figure 2.1: Physical characterization of electrospun scaffolds..... 31

Figure 2.2: Cells are viable and proliferative independent of PEDOT:PSS concentration. 32

Figure 2.3: RNA sequencing identifies upregulation of cardiac-related genes on conductive substrates..... 33

Figure 2.4: Structural characterization of hPSC-CMs. 34

Figure 2.5: hPSC-CM calcium handling on conductive PEDOT:PSS/PVA electrospun scaffolds. 35

Figure 2.6: hPSC-CM action potentials on conductive PEDOT:PSS/PVA electrospun scaffolds. 36

Figure 3.1: Microfiber and cardiac spheroid formation..... 55

Figure 3.2: Cardiac spheroid contractility parameter change over time..... 56

Figure 3.3: Cardiac spheroid compaction over time..... 57

Figure 3.4: Cardiac protein expression increases in conductive cardiac spheroids..... 58

Figure 3.5: Calcium handling performance of cardiac spheroids..... 59

Supplemental Figure 2.1: Experimental setup for TLM measurements on electrospun scaffolds. 37

Supplemental Figure 2.2: hPSC-CM morphology. 37

Supplemental Figure 2.3: hPSC-CM purity. 38

Supplemental Figure 3.1: Percentage of beating cardiac spheroids with varying fiber mass or length over 15 days. 61

Supplemental Figure 3.2: MYH7 expression for cardiac spheroids. 62

LIST OF TABLES

Table 3.1: Cell number per cardiac spheroid for each condition across three biological replicates. 60

LIST OF SUPPLEMENTAL FILES

Supplemental Table 2.1: Gonzalez_VolcanoPlot.xlsx

Supplemental Video 3.1: Gonzalez_3DCtrl_CalciumFlux.avi

Supplemental Video 3.2: Gonzalez_PVA_CalciumFlux.avi

Supplemental Video 3.3: Gonzalez_PEDOTPSS_CalciumFlux.avi

ACKNOWLEDGEMENTS

I would like to thank Dr. Adam Engler for the opportunity to join his lab and mentoring me in becoming an independent scientist. In addition, I would like to thank the members of the Engler lab for training me in the scientific techniques needed to fulfill my degree. Particularly, I would like to acknowledge Erin LaMontagne, Alyssa Holman, Aileena Nelson, Thomas Molley, Alexander Whitehead, and Hamza Atcha for their guidance and support. I would also like to thank my undergraduate mentee Rachel Lian, who aided in my cardiac differentiations, electrospinning, and provided moral support during difficult experiments. I would also like to thank my thesis committee – Dr. Brian Aguado, Dr. Shaochen Chen, and Dr. Shadi Dayeh – for their scientific input, expertise, and challenging me to critique the results of my work. I would also like to thank my funding sources – NSF GRFP, San Diego Fellowship, and the Siebel Scholar Foundation – for the financial support to complete this degree. Finally, I would like to thank my friends and family. I started this graduate school journey with Marianne Madias, whom I met during my freshman year of college, and we will now be completing our PhD at the same time. I could not have asked for a better friend to grow with throughout this process. Further, I would like to thank my older sister, Evelyn, whose dedication to education I have always admired was always there for me when I needed a break. Lastly, I have dedicated this thesis to my parents, both immigrants from Mexico, for the sacrifices they made and their endless support in pursuing my career.

Chapter 1, in full, is a reprint of the following material of which the dissertation author was one of the primary investigators and authors of this paper, equally contributing with Aileena C. Nelson and Alyssa R. Holman. Gonzalez G, Holman AR, Nelson AC, Engler AJ. Engineering the niche to differentiate and deploy cardiovascular cells. Curr Opin Biotechnol. 2022;74:122-128. doi:10.1016/j.copbio.2021.11.003.

Chapter 2, in full, is a reprint of the material as it appears in Biomaterials. Gonzalez G, Nelson AC, Holman AR, Whitehead AJ, LaMontagne E, Lian R, Vatsyayan R, Dayeh SA, & Engler AJ. Conductive electrospun polymer improves stem cell-derived cardiomyocyte function and maturation. Biomaterials. 2023;302:122363. doi:10.1016/j.biomaterials.2023.122363. The dissertation author was the primary investigator and author of this paper. The authors would like to thank Dr. Neil Chi (UCSD) for the donation of the RUES2 ESCs, Dr. Karen Christman (UCSD) for access to the BioTek plate reader, Dr. Kristen Jepsen of the Institute for Genomic Medicine (UCSD) for technical assistance with sequencing, Dr. Elsa Molina (Sanford Consortium Stem Cell Core) for access and maintenance of the LSM 780 microscope, and Dr. Max Rempel (Sanford Consortium Stem Cell Core) for access and maintenance of the Andor Dragonfly microscope. This work was performed in part at the San Diego Nanotechnology Infrastructure (SDNI) of UCSD, a member of the National Technology Coordinated Infrastructure (NNCI), which is supported by the National Science Foundation (ECCS-2025752). The authors acknowledge funding and equipment support from the National Institutes of Health (R01AG045428 to A.J.E. and DP2EB029757-01 to S.A.D.). Fellowship support was provided by the American Heart Association (20PRE35180060 to A.C.N.), the National Science Foundation (to G.G., E.L., and A.J.W.), the San Diego Fellowship (to G.G.), and the National Institutes of Health (F31 HL163996 to A.R.H.).

Chapter 3, in full, is currently being prepared for publication. Gonzalez G, Holman AR, LaMontagne E, Molley TG, Engler AJ. Conductive microfibers improve stem cell-derived cardiac spheroid maturation. The dissertation author was the primary researcher and author of this paper. The authors would like to thank Dr. Neil Chi (UCSD) for the donation of the RUES2 ESCs, Dr. Karen Christman (UCSD) for access to the Olympus microscope, Dr. Max Rempel (Sanford

Consortium Stem Cell Core) for access and maintenance of the Keyence microscope, and Dr. Brian Aguado for access to the Leica cryostat. The authors acknowledge funding and equipment support from the National Institutes of Health (R01AG045428 to A.J.E.). Fellowship support was provided by the National Science Foundation (to G.G. and E.L.), the San Diego Fellowship (to G.G.), and the National Institutes of Health (F31 HL163996 to A.R.H.).

VITA

2019 Bachelor of Science in Biomedical Engineering, The University of Arizona

2024 Doctor of Philosophy in Bioengineering, University of California San Diego

PUBLICATIONS

Gonzalez G, Holman AR, LaMontagne E, Molley TG, Engler AJ. Conductive microfibers improve stem cell-derived cardiac spheroid maturation. In preparation.

LaMontagne E, **Gonzalez G**, Vatsyayan R, Burgos-Marin B, Puppo F, Biagi D, Dayeh SA, Muotri AR, Engler AJ. Graphene-polymer nanofibers enable optically induced electrical maturation in stem cell-derived cardiomyocytes and brain organoids. Nature Materials. 2024, in review.

Ren Y, De-Eknamkul C, Sun F, Ramezani M, **Gonzalez G**, Huang W, Wilson M, Engler AJ, Kuzum D, Cubukcu E. Trionic label-free all-optical biological voltage sensing via quantum statistics. Science. 2024, in review.

Gonzalez G, Nelson AC, Holman AR, Whitehead AJ, LaMontagne E, Lian R, Vatsyayan R, Dayeh SA, & Engler AJ. Conductive electrospun polymer improves stem cell-derived cardiomyocyte function and maturation. Biomaterials. 2023;302:122363. doi:10.1016/j.biomaterials.2023.122363. The dissertation author was the primary investigator and author of this paper.

Gonzalez G, Holman AR, Nelson AC, Engler AJ. Engineering the niche to differentiate and deploy cardiovascular cells. Curr Opin Biotechnol. 2022;74:122-128. doi:10.1016/j.copbio.2021.11.003.

ABSTRACT OF THE DISSERTATION

Conductive polymers improve human stem cell-derived cardiomyocyte function in two-dimensional and three-dimensional cultures

by

Gisselle Gonzalez

Doctor of Philosophy in Bioengineering

University of California San Diego, 2024

Professor Adam J. Engler, Chair

Given the prevalence of cardiovascular disease (CVD) worldwide and in the US, there is a need for mature cardiac models that recapitulate the disease complexity and function of native cardiac tissue. Conventional two-dimensional (2D) human pluripotent stem cell-derived cardiomyocyte (hPSC-CM) differentiations fail to achieve the maturity levels of more intricate three-dimensional (3D) cardiac models. hPSC-CMs often remain immature, electrically isolated, and may not reflect adult biology. Conductive polymers are attractive candidates to facilitate

electrical communication between hPSC-CMs, especially at sub-confluent cell densities or diseased cells lacking cell-cell junctions. Here, we investigated how conductive polymers may be used to facilitate electrical communication between hPSC-CMs in both 2D and 3D platforms to create functionally mature cardiomyocytes for disease modeling and potential therapeutics. First, we summarized past, current, and future engineering methods implemented to direct hPSC-CM differentiations to recapitulate the complexity of native cardiac tissue. Next, we developed conductive electrospun fibrous scaffolds and assessed the structural, functional, and transcriptional changes of hPSC-CMs seeded on a 2D network. Lastly, we translated our 2D findings to 3D cardiac spheroid models to investigate how the presence of conductive microfibers may accelerate cardiac spheroid maturation over standard 3D models. Taken together, these data suggest that conductive polymer platforms are supportive of electrical coupling in hPSC-CMs and promote maturation, which may improve our ability to model cardiac diseases and develop targeted therapies.

Chapter 1 Engineering the niche to differentiate and deploy cardiovascular cells

1.1 Abstract

Applications for stem cells have ranged from therapeutic interventions to more conventional screening and *in vitro* modeling, but significant limitations to each is due to the lack of maturity from decades old monolayer protocols. While those methods remain the 'gold standard,' newer three-dimensional (3D) methods, when combined with engineered niche, stand to significantly improve cell maturity and enable new applications. Here in three parts, we first discuss past methods, and where and why we believe those methods produced suboptimal myocytes. Second, we note how newer methods are moving the field into an era of cell mechanical, electrical, and biological maturity. Finally, we highlight how these improvements will solve issues of scale and engraftment to yield clinical success. It is our conclusion that only through a combination of diverse cell populations and engineered niche will we create an engineered heart tissue with the maturity and vasculature to integrate successfully into a host.

1.2 Introduction

For more than two decades since the initial isolation of human pluripotent stem cells (hPSCs), and even more so with the advent of human induced pluripotent stem cells (hiPSCs), the stem cell and cardiovascular fields have developed protocols to differentiate cells into cardiomyocytes (CMs). hPSC-progeny and hiPSC-progeny have been used in a variety of applications ranging from therapeutic applications[1,2] in the failing heart to mechanisms of action studies in disease-in-a-dish models[3]. To develop as many cells as possible for these applications, most protocols have relied on feeder layer-free monolayer culture methods with chemically

defined media, which achieve reproducible, near homogeneous cardiomyocyte populations, for example, 10^6 myocytes/cm^2 or >90% efficiency in a matter of days. More recently, protocols have included negative selection to kill cells not metabolically mature[4] or to express genetically encoded reporters and positive selection to guide cells towards mature subtypes via mechanically and electrically defined niche. These protocols can be massively scaled up and enable labs to create 10^8–10^{11} cells required for therapeutic applications in large mammals[1]. However, they do not create functionally mature atrial or ventricular subtypes as well as the non-cardiac subtypes that can account for up to 70% of all myocardial cells *in vivo*. A combination of 3D maturation with many supporting cell types and further engineering of the niche may more appropriately signal to cells and push myocytes into these subtypes. As the field begins to recognize this problem[5], we briefly review and then provide detailed opinion on: (i) where did the field 'go wrong' when trying to produce mature ventricular myocytes, (ii) how can the field correct itself and produce these cells, and (iii) how can we use these more mature cells for new approaches to improve disease? With this review, we hope that these sections inform but also describe the direction we believe the field should pursue to maximize opportunities for cardiac regeneration.

1.3 Results

1.3.1 Where did we go wrong?

hPSCs, including embryonic (hESC) and induced (hiPSC), have a vast potential as a cell replacement source due to their indefinite self-renewal capacity and ability to be reprogrammed or derived from patient cells[4,6]. Numerous studies have demonstrated that hPSC-derived CMs have the ability to survive and engraft within host tissue, but these cells are typically a mixed population of immature CMs including atrial, ventricular, and pacemaker-like cells which can lead to altered cardiac physiological behavior such as arrhythmias[1,2,7–9]. Therefore, it is of great importance to

understand how to best recapitulate the cardiac cell states present in the heart utilizing the appropriate cellular cues.

Originally, mouse stem cells were differentiated into CMs by generating multicellular aggregates called embryoid bodies (EBs), since they can form all three germ layers, which then produce spontaneously contractile regions consisting of a low number of CMs[10,11]. As more information was uncovered about the process of cardiogenesis, growth factors were utilized to direct the differentiation of stem cells into CMs in a more efficient manner. Currently, two predominant methods exist for differentiating hPSCs into CMs — 2D and 3D models. Protocols of both systems are based on heart formation *in vivo*, beginning with the differentiation of pluripotent cells into the mesoderm germ layer, then into the specific cardiac lineages. This process is done by modulating the Wnt pathway using small molecules including Wnt/β-catenin activators such as Gsk3β inhibitors (e.g. CHIR99021, BIO, etc.) and BMPs, and Wnt inhibitors (e.g. IWR1, WNT-C59, XAV939, etc.)[12,13]. The more common system is a 2D monolayer protocol, which gives rise to CMs consistently and efficiently[4,6]. The 2D system was introduced in Mummery *et al.* where hPSCs were co-cultured with an endodermal cell line, which cleared insulin thereby allowing for cardiac induction[14]. Future studies built on this protocol by utilizing an insulin-free media along with either WNT-driven or BMP-driven differentiations[15]. While these protocols have proved successful in generating CMs, the 2D protocol generates an immature population of CMs that does not adequately mimic the electrical, mechanical, chemical, or organizational properties of the human heart, thus there is vast room for improvement to this model[16–18]. For these reasons, a subset of the field has employed a 3D model to generate CMs[19–22], but these models are not as efficient or reproducible and are more complicated to execute. Despite this, there is growing evidence suggesting that 3D models influence cardiac maturation more than the 2D system; thus,

3D systems have the potential to generate higher proportions of functional and mature CMs[23,24]. The increased maturity of 3D-derived CMs has been attributed to differences in morphology, spatial organization, biochemical signals, and electrical and mechanical loading due to both direct and indirect interactions between CMs and other cardiac cell types, including endothelial cells and fibroblasts[25–28] (Figure 1.1). However, there is still room for improvement in these 3D models as high capacity electrical and mechanical outputs, metabolic maturity markers, and mature cellular structure and morphology are missing that are present for *in vivo* human CMs[16,17]. Thus to recapitulate the maturity of CMs seen *in vivo* and capture the mature aspects of the 3D-based hPSC-CM protocol, there needs to be an emphasis on utilizing cellular interactions, specifically chemical and physical cues, to better mature CMs.

Recent studies have further explored the role of cell–cell communications on cardiac maturation. For instance, signaling between non-CM cell types, for example, endothelial cells and fibroblasts, and CMs has been identified as crucial for cardiac maturation[29,30]. One study found that the co-culture of hiPSC-CMs and endothelial cells upregulated cardiac hormones and cardioprotective factors, while also increasing structural maturity and extracellular matrix deposition in hiPSC-CMs[30]. Another study found that VEGF-VEGFR2 signaling between non-CMs (endothelial cells and fibroblasts) and CMs led to increased expression of gap junction proteins and contractile function[31]. These findings demonstrate that physical and biochemical signaling from distinct cardiac cell types assists in generating mature CMs. While it would be ideal to recapitulate all of the cell types of the human heart, it is infeasible; thus these biochemical and physical cues can be applied to CMs ectopically to induce a more functionally mature population of CMs.

1.3.2 How are we trying to get it right?

Material stiffness

In addition to biochemical cues and paracrine signaling that come with 3D multi-cellular cultures, recent efforts have included the combination of structural and functional stimuli to aid *in vitro* cardiac maturation. Extracellular matrix (ECM) stiffness and composition, among other cues, have a direct impact on stem cell fate and hPSC-CM function[32–35]; many groups have utilized biomaterials that recapitulate the stiffness and composition of the native cardiac microenvironment to create cardiac tissue engineering models. Collagen-based scaffolds are attractive due to their biocompatibility, mechanical strength, and the abundance of collagen type I within the heart[36,37] whereas the viscoelasticity and bioactivity of fibrin hydrogels can be equally useful for cardiac tissue constructs[38]. Conversely synthetic polymers, for example, poly(ethylene glycol) (PEG), poly(lactic-co-glycolic acid) (PLGA), and poly(caprolactone), provide a biocompatible environment with controlled degradation rates and tunable mechanical properties that can be temporally manipulated to match *in vivo* stiffness during development[32]. While material stiffness can provide mechanical cues for 2D cell cultures, stretch of compliant biomaterials, such as polydimethylsiloxane (PDMS), can drive active remodeling in 3D cardiac tissue constructs; uniaxial CM tension can be driven by stretching PDMS and active responses can be modulated by tuning the stiffness and length of PDMS posts to which cells adhere[39]. These posts can even mirror the effects of afterload on engineered heart tissues (EHTs), that is, heart wall stress during ventricular contraction, when they bind to one rigid and one flexible post; moderate afterload increases maturation markers[40]. Further examples of mechanical stimulation methods for cardiac maturation have been described elsewhere[41].

Electromechanical stimulation and multicellularity

Researchers have also explored the use of conductive materials to potentially improve hPSC-CM electrical maturation even when there is minimal cell–cell contact[42–45]. For example when Ruan *et al.* implemented static stress and electrical stimulation to hPSC-CM/collagen constructs, they found an increase in the overall stress production compared to unconditioned constructs (1.34 mN/mm^2 versus 0.055 mN/mm^2), as well as an increase in *SERCA2* and *RYR2* expression, which are necessary for proper calcium handling and electrical function[46]. Electrical signals can also be propagated within the conductive polymer poly(3,4 ethylenedioxythiophene) (PEDOT), and for hiPSC-CMs, electrical stimulation improves sarcomere formation and contraction velocity and amplitude compared to non-conductive materials without external stimuli[43]. Conductive graphene oxide can also improve expression of cardiac genes related to contractile and electrophysiological function in hiPSC-CMs[42]. Given the importance of electrical signaling in heart development, researchers have explored electrical stimulation for cardiac maturation[47,48]. Radisic *et al.* electrically stimulated neonatal CMs in 2D culture and found improved ultrastructure organization, increased levels cardiac maturation markers such as *cTnI* and *Cx43*, and greater contraction forces compared to non-stimulated cultures; the findings of this work have served as the basis for hPSC-CM electrical maturation[48].

Each of the examples above used complex engineered systems but employed cells derived from monolayers, thus having only a single cell type present. While monolayer methods are still clearly the dominant method, several newer cardiac tissue construct examples employ heterogeneous EB methods, showing further improvements in cell maturity and could be a sign of the field 'correcting' itself. hPSC-CMs dissociated from EBs, combined with conductive Biowire, and trained with increased stimulation frequency over one week led to improved ultrastructure organization, calcium handling, and electrophysiological maturity[47]. Electromechanical intensity

training has even further advanced maturity levels[24,46,48–50]. For example, Llucia-Valldeperas *et al.* investigated the effects of 2D electromechanical stimulation, albeit on adipose-derived and not hiPSC-derived or hPSC-derived CMs[49]. Immature EHTs containing multiple cell types have also been suspended between flexible PDMS posts, stimulated from 2 to 6 Hz and then maintained at 2 Hz. These EHTs formed a significant number of T-tubules for calcium handling and showed the first positive force frequency relationship in an hPSC-derived model, although maximum force was 10-fold lower than *in vivo* (4 mN/mm^2 versus 40 mN/mm^2)[24]. These works demonstrate the importance of various niche stimuli for hPSC-CM maturation along with requiring a diverse population of supporting cells; this combined approach, which we believe needs to become standard in the field, is summarized in Figure 1.2.

1.3.3 How can we translate new approach to humans?

While recent advances in hPSC technology, differentiation methods, and biomaterial applications could push cell maturity, the lack of easy scalability could prevent significant clinical applications in humans and limit hPSC-CM approaches to disease modeling and screening. With 10^8–10^{11} cells required for therapeutic applications[1], producing large quantities of CMs required for transplantation[51,52] and achieving their successful engraftment[53] could prove a significant impediment. Continued improvements in CM differentiation efficiency and maturation, and a greater understanding of other endogenous cell populations could greatly improve regenerative strategies for patients[54,55].

While 2D and 3D protocols have been shown to effectively generate CMs from hPSCs[4,6,19] the generation of therapeutically relevant numbers of CMs remains challenging. Recent studies have focused on modulating Wnt and Hippo pathways in monolayer cultures[55] to induce large-scale hPSC-CM expansion in bioreactors. Molecules previously identified in promoting CM

proliferation[56,57], when applied *in vitro* in combination with cell contact inhibition, can robustly generate 10^9 hPSC-CMs necessary for therapeutic approaches[55], but the tradeoff is cell maturation. Conversely, suspension culture-based strategies[58,59] suffer from low CM efficiency and cell death[60]. To overcome that limitation, hPSCs were formed into aggregates and differentiated via canonical Wnt modulators in an approach that allows for >80% CM purity without the need for further lineage enrichment[60]. While 2D and 3D suspension culture methods can produce large quantities of hPSCs, additional mechanical and electrical stimuli should be employed to ensure the functional maturity of hPSC-CMs.

Delivery and engraftment of these vast numbers of hPSC-CMs remains a second critical issue. Of all the potential solutions, we believe that direct live cell and ECM printing is most promising. 3D bioprinting improves upon the decades-old approach of loading cells onto biocompatible scaffolds to offer precise control of construct architecture and biological function, as described at greater length by Zhang *et al.*[61]. While it has proved to be a challenge in the past, due to difficulties in maintaining structural support during printing[62,63], novel methods such as the freeform reversible embedding of suspended hydrogels (FRESH) provides the precise control that could overcome these limitations. FRESH printing provides mechanical support for printed filaments by printing into a bath of spherical gelatin microparticles that can be melted at 37°C after printing[62]. In addition to printing, perfusable vascularized networks could further promote hPSC-CM engraftment and anastomosis with the host vasculature[37,51], for example, the sacrificial writing in functional tissue (SWIFT) method where organoid bodies are populated throughout matrices through which perfusable channels are introduced via 3D printing[51]. These next generation printing methods may improve engraftment, but as mentioned before, cell populations must recapitulate the cell diversity found in the ventricle wall.

To bridge the gap between current hPSC technologies and cardiac regenerative therapies, robust cellular differentiation protocols and engineered tissues recapitulating the vascular networks and cellular composition of native niches must be achieved. Recent advances in differentiation methodology, orchestration of biomechanical and chemical cues, and 3D bioprinting represent promising pathways for overcoming this challenge[64,65]. However as articulated here, we believe that much is left to do before and if engineered cardiovascular tissues can be deployed in a clinical setting.

1.4 Conclusion

One significant goal for the field of stem cell-derived myocytes has been to create enough mature cells for cardiac regeneration. As we noted at the outset in trying to create the most efficient monolayer differentiation protocol, the field lost track of the basic developmental biology that should guide cardiomyocyte differentiation and maturation into adult cardiac phenotypes. By turning to maturation methods where a diverse cell population is present, we can create a CM subpopulation that is more mature and better specified for specific jobs within the myocardium. However, this recent shift in thinking must be coupled to a decades long effort to improve the myocyte cell niche; only through the combination of defined matrix properties and a diverse cell population will sufficiently mature cells be produced. Of course once this process can be scaled up, only then will regenerative therapies for hPSC-based and hiPSC-based CMs be possible.

1.5 Figures

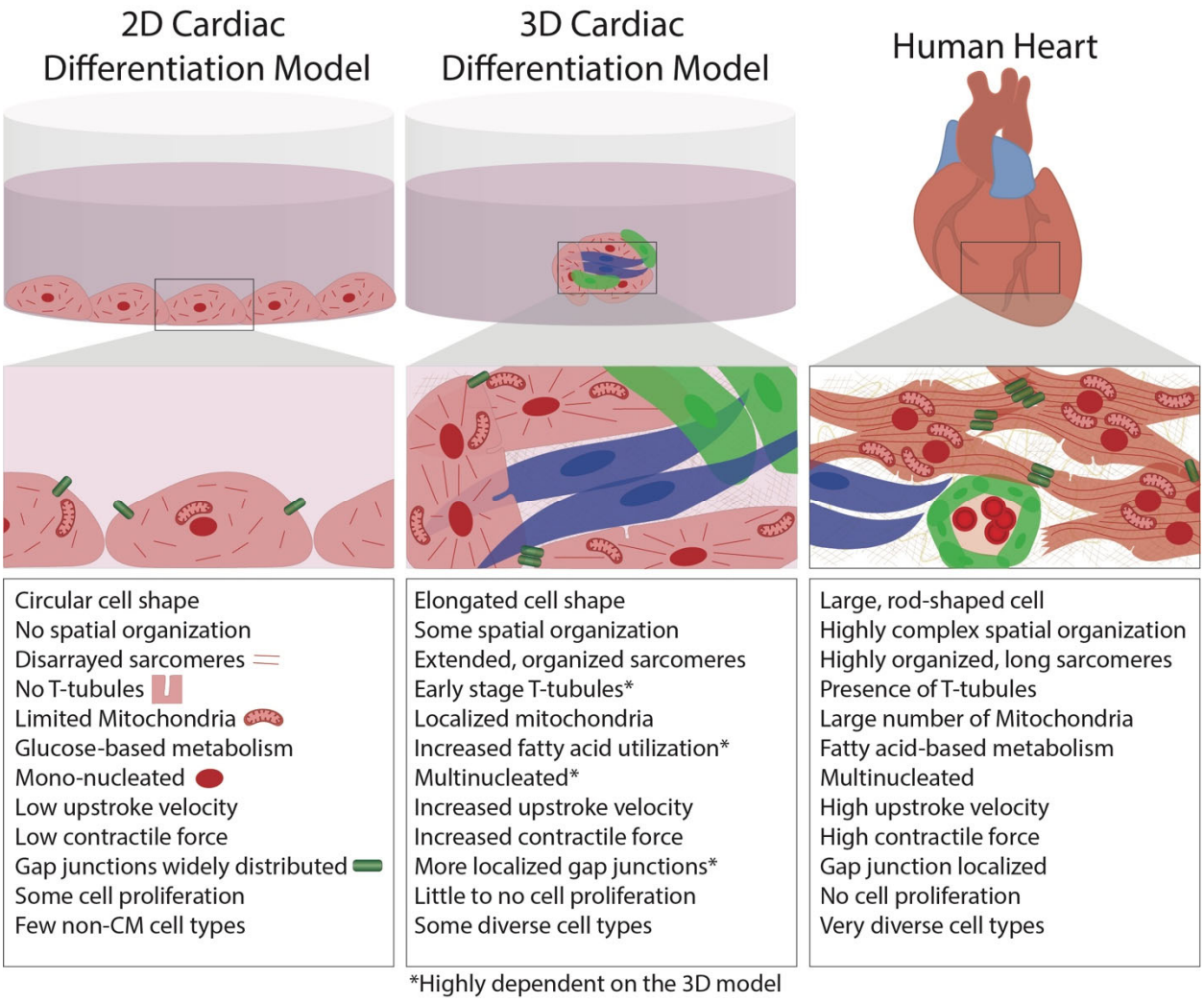


Figure 1.1: *In vitro* differentiation methods and their comparison to *in vivo* cardiac tissues.

Schematic and lists indicate how the differentiation methods differ, both in approach as well as in cellular outcomes. Both are compared to native myocardium. Cell types and intracellular structures drawn in the figure are noted in the key at bottom with descriptions of the cell state in the models. Note that for the 3D system, * indicate that the cell structure is dependent on model parameters and can vary widely between systems and users.

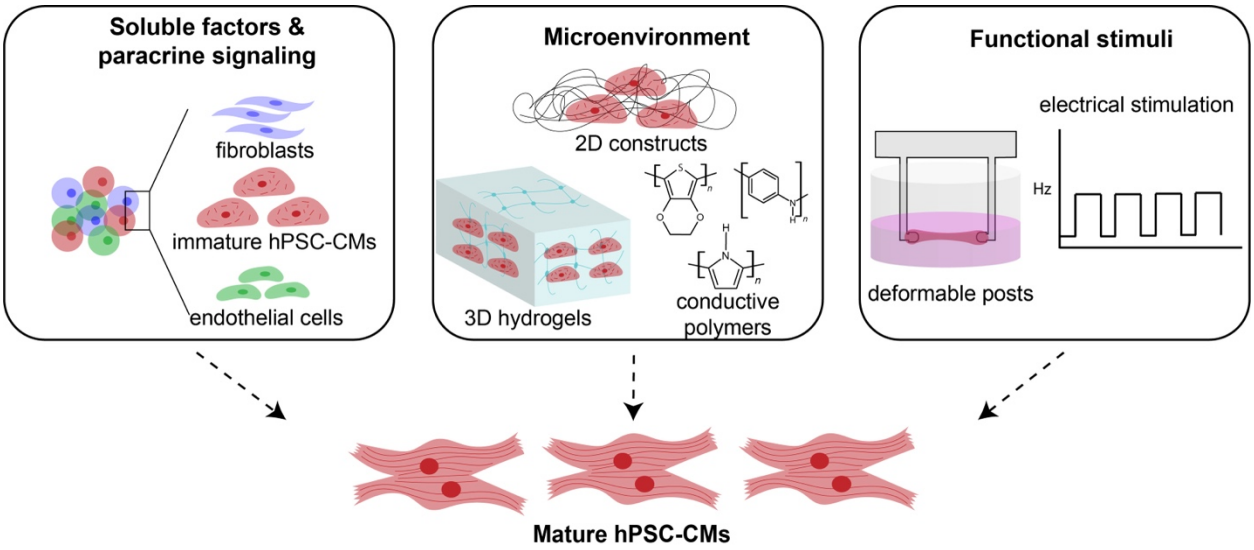


Figure 1.2: Engineered cues presented to hPSC-derived myocytes.

Schematic indicating diverse cell populations providing soluble and cell–cell-based factors to improve CM maturation (left). This can be augmented by passive (center) and active (right) insoluble extracellular cues, for example, biomaterials, stretch, electrical stimulation, and so on.

1.6 Acknowledgements

Chapter 1, in full, is a reprint of the following material of which the dissertation author was one of the primary investigators and authors of this paper, equally contributing with Aileena C. Nelson and Alyssa R. Holman. Gonzalez G, Holman AR, Nelson AC, Engler AJ. Engineering the niche to differentiate and deploy cardiovascular cells. Curr Opin Biotechnol. 2022;74:122-128. doi:10.1016/j.copbio.2021.11.003.

Chapter 2 Conductive electrospun polymer improves stem cell-derived cardiomyocyte function and maturation

2.1 Abstract

Despite numerous efforts to generate mature human pluripotent stem cell-derived cardiomyocytes (hPSC-CMs), cells often remain immature, electrically isolated, and may not reflect adult biology. Conductive polymers are attractive candidates to facilitate electrical communication between hPSC-CMs, especially at sub-confluent cell densities or diseased cells lacking cell-cell junctions. Here we electrospun conductive polymers to create a conductive fiber mesh and assess if electrical signal propagation is improved in hPSC-CMs seeded on the mesh network. Matrix characterization indicated fiber structure remained stable over weeks in buffer, scaffold stiffness remained near *in vivo* cardiac stiffness, and electrical conductivity scaled with conductive polymer concentration. Cells remained adherent and viable on the scaffolds for at least 5 days. Transcriptomic profiling of hPSC-CMs cultured on conductive substrates for 3 days showed upregulation of cardiac and muscle-related genes versus non-conductive fibers. Structural proteins were more organized and calcium handling was improved on conductive substrates, even at sub-confluent cell densities; prolonged culture on conductive scaffolds improved membrane depolarization compared to non-conductive substrates. Taken together, these data suggest that blended, conductive scaffolds are stable, supportive of electrical coupling in hPSC-CMs, and promote maturation, which may improve our ability to model cardiac diseases and develop targeted therapies.

2.2 Introduction

Since the early efforts in differentiating human pluripotent stem cells into cardiomyocytes (hPSC-CMs), their potential to study various cardiovascular diseases and their use as a therapeutic for diseases has been greatly explored[1–3]. While initial studies aimed to differentiate hPSC-CMs in two-dimensional (2D) monolayers and maximize cell population purity[4,5], current efforts strive to generate more mature cells by recapitulating the complexity of native cardiac tissue[6,7]. Previous studies indicate that hPSC-CM maturation requires paracrine signaling between various cell types that compose cardiac tissue[8], a tissue-relevant microenvironment conducive to cellular communication[9], and more recently, electrical and mechanical stimulation[10]. However, despite many efforts to achieve mature cells, hPSC-CMs remain immature, exhibit poor sarcomere organization important for contractility, experience asynchronous contractions, and fail to replicate metabolic activity levels of native cardiomyocytes[6].

Biomaterials are being explored as methods to address these problems and enhance overall cardiac tissue maturation. Most biomaterials create an insulating environment, which may impede electrical propagation, but recently, conductive materials[66] have been substituted to improve electrical maturation and signal propagation between cells. Polypyrrole (PPy) and polyaniline (PANI) are among the most studied conductive polymers[67–71], but these materials are difficult to disperse in an aqueous environment and are cytotoxic, raising concerns for their long-term use in physiological conditions[72]. In contrast, poly(3,4-ethylenedioxythiophene) poly(styrene sulfonate) (PEDOT:PSS) has recently been shown to be conductive in an aqueous environment[72] whereas PPy and PANI are not. PEDOT:PSS biocompatibility may be more limited than other PEDOT derivatives[73,74], but when blended with other polymers, such as poly(vinyl) alcohol (PVA) and a poly(ethylene glycol) (PEG)-based crosslinker[75], PEDOT:PSS may exhibit improved chemical

stability and biocompatibility. Likewise, the addition of synthetic biocompatible polymers can further tune mechanical properties, such as degradation rate and stiffness, of PEDOT:PSS products to better mimic the native cardiac tissue environment. Alongside composition, these materials can be configured as nanofibers by electrospinning[19] to better simulate the fibrous extracellular matrix (ECM) structure of native tissues. By electrospinning blends of biocompatible and conductive polymers, a tunable, conductive environment for hPSC-CM maturation and function may be possible.

Cardiomyocytes in the heart exist in three-dimensional layers, interrupted by sporadic cardiac fibroblasts, immune cells, blood vessels, and ECM, among other constituents. A conductive polymer may be able to propagate signals and synchronous contraction even in sub-confluent monolayers of hPSC-CMs as would occur between layers in the heart. To assess the degree to which this was possible, we first evaluated the material properties and biocompatibility of electrospun PEDOT:PSS/PVA scaffolds. In hPSC-CMs, conductive substrates increased expression of cardiac related genes as well as the localization and organization of junction and structural proteins, such as desmoplakin (DP) and α-actinin, respectively. Higher cardiac gene expression and improved structure led to more coordinated calcium handling, even in sub-confluent hPSC-CM layers. Prolonged hPSC-CM culture on conductive scaffolds demonstrated higher cell retention and action potential intensities, overall suggesting that conductive polymer networks may improve function and contribute to the maturity of hPSC-derived cardiac tissue constructs.

2.3 Materials and methods

2.3.1 Preparation of PVA/PEDOT:PSS/PEGDE solutions

PVA (Sigma-Aldrich, 363146) was dissolved in deionized (DI) water at a 20% (w/v) at 130ºC under magnetic stirring for 3 hours. Poly(ethylene glycol) diglycidyl ether (PEGDE, Sigma-Aldrich, 475696) was mixed with PEDOT:PSS 1.3% wt. dispersion in water (Sigma-Aldrich, 483095) at a 3% (w/v) concentration as described by Solazzo et al[75]. The 3% PEGDE/PEDOT:PSS solution was vortexed for 30 seconds, sonicated for 30 minutes, and syringe filtered with a 0.45µm filter (Corning, 431225) to remove aggregates. The resulting solutions were combined to create base 8% (w/v) PVA solutions with 0%, 3.25%, 6.5%, and 9.75% mass to mass ratio solutions of PEDOT:PSS to PVA. A mass-matched solution of 11% (w/v) PVA was created to match the polymer mass of the 9.75% solution. Solutions were vortexed for 1 hour to form a homogeneous mixture and desiccated for 1 hour to remove air bubbles.

2.3.2 Composite PVA/PEDOT:PSS/PEGDE electrospun scaffold fabrication

An Inovenso Nanospinner (KTP700 Basic) electrospinner was utilized for scaffold fabrication at 0.5-0.75mL/hr flow rate, 20cm working distance, 33kV applied voltage, and 30% humidity with a 0.8mm nozzle for a total of 0.1mL solution spun per session. Scaffolds were collected on 18 mm coverslips (Fisherbrand, 12545100) for scanning electron microscopy (SEM), atomic force microscopy (AFM), and biological experiments and on 24x40mm coverslips (Fisherbrand, 12545D) for conductivity measurements. To crosslink the polymers, scaffolds were placed in a glass chamber (Chemglass, AF-0556) in the presence of 0.2M glutaraldehyde, subjected to vacuum for 15 seconds, and placed in an oven at 80ºC for either 15 or 30 minutes. After crosslinking, scaffolds were washed three times for 30 minutes with a 1% (w/v) glycine solution to remove unreacted glutaraldehyde, followed by three 10-minute washes in DI water[76]. Crosslinked scaffolds were dried at room temperature overnight prior to use.

2.3.3 Scaffold degradation and fiber morphology

After either 15 or 30 minutes of crosslinking, 8% w/v PVA electrospun scaffolds were incubated in DPBS (1X) (Gibco, 14190-144) at 37ºC over 4 weeks. Scaffolds containing 9.75% PEDOT:PSS/PVA crosslinked at 30 minutes were also incubated to investigate the degradation of conductive scaffolds. Scanning electron microscopy (SEM) images of scaffolds immediately before and after crosslinking, as well as after 1, 2, or 4 weeks of incubation were obtained on a Zeiss Sigma 500 SEM. The scaffolds were mounted on carbon-taped standard aluminum stubs and sputter coated with iridium to reduce electron charging on the sample surface. A working accelerating voltage of 3kV and an objective aperture of 30µm were utilized for all samples. Three images per scaffold at each timepoint were obtained. SEM images obtained at 10k magnification were analyzed on ImageJ to determine the average electrospun fiber diameter over time. Three images per scaffold and 10 fibers per image were measured. In instances where the fibers annealed and formed a film, the fiber diameter was not measured.

2.3.4 Bulk stiffness

Bulk stiffness after 30 minutes of crosslinking was measured using an Oxford Instruments MFP-3D Bio atomic force microscope (AFM). Scaffolds with an 8% PVA base containing 0%, 3.25%, 6.5% and 9.75% PEDOT:PSS/PVA as well as a mass-matched 11% w/v PVA scaffold were soaked for 1 hour in DPBS prior to AFM and maintained in DPBS during measurements. A silicon nitride cantilever with a 45 µm polystyrene bead tip and 0.03N/m stiffness (Novascan) was utilized with a scan rate of 8kHz, 1 nN trigger force, 2µm/s velocity, and 3µm force distance. Three force maps of 20x20µm with a total of 20 points per force map were obtained per sample, with 4 scaffolds per group. Force maps were analyzed by fitting a Hertz model to the curves[77].

2.3.5 Conductivity measurements

Transfer Length Method (TLM) measurements were performed to determine the sheet conductivity. Autodesk AUTOCAD was used to create a software mask, which was patterned on polyethylene terephthalate (PET) tape using a Universal Laser Systems VLS3.60DT laser cutter to create a shadow mask for metal deposition directly on electrospun scaffolds via electron beam (e-beam) evaporation. 50 nm thick Gold (Au) rectangular contacts with 1 cm width were deposited on the scaffolds with inter-contact spacings of 500, 1000, 2000, 3000, 4000 and 5000 μm. Current-voltage measurements for inter-contact resistance evaluation were conducted using an Agilent B1500A Semiconductor Device Analyzer. In TLM, the resistance between contact pairs provides a measure of the contact resistance between the Au and the scaffolds (independent of inter-contact spacing) and total scaffold film resistance between the contacts (linearly dependent on inter-contact spacing). The sheet resistance may be calculated from the slope of the line-fit when plotting resistance against inter-contact spacing from:

$$slope = \frac{R_{sh}}{W} \quad (1)$$

where R_{sh} is the sheet resistance (Ω sq^{-1}) and W is the Au contact width[78,79]. The final material conductivity was calculated by:

$$\sigma = \frac{1}{R_{sh} \cdot t} \quad (2)$$

where σ is conductivity (S/cm) and t is the electrospun scaffold thickness. To measure thickness, scaffolds were hydrated, cut to create a height difference between the scaffold and glass substrate and measured via a Dektak XT Stylus Profilometer (Bruker) with a 12.5μm stylus tip radius, 3mg stylus force, and 6.5μm range.

2.3.6 Scaffold sterilization and NIH/3T3 cell culture

Scaffolds containing increasing PEDOT:PSS suspended on 18mm coverslips were crosslinked for 30min and sterilized under UV for 1h on either side, transferred to 12 well plates,

and washed with sterile DPBS three times to remove debris. A 0.1% (w/v) gelatin-coated glass substrate was used as a positive control in all experiments, while an 11% PVA scaffold was used as a mass-matched control. NIH/3T3 embryonic mouse fibroblasts were seeded at a concentration of 20,000 cells per well. Media composed of DMEM (Dulbecco's Modified Eagle Media; Gibco, 11966025), 10% (v/v) fetal bovine serum (FBS) (Omega Scientific, NC0471611), and 1% (v/v) penicillin/streptomycin (Gibco, 15070063) was changed daily.

2.3.7 Cell viability assays

Material cytotoxicity was determined via a LIVE/DEAD Viability/Cytotoxicity kit (Invitrogen, L3224). Cells adhered onto each substrate for 24–120h, were washed with DPBS, then incubated in 2μM calcein-AM and 4μM ethidium-homodimer-1 in DPBS for 30min at room temperature. Scaffolds were inverted onto a 35mm glass bottom culture dish (MatTek, P35G-0-20-C) and sealed with Parafilm to prevent solution evaporation. A Nikon Eclipse Ti microscope with a Yokogawa CSU-X1 confocal attachment was used to image the percentage of live and dead cells. ImageJ was used to quantify the percentage of live to dead cells at 1 and 5 days after cell seeding. Alternatively, cells were stained with Ki67 (1:800, Invitrogen, 14-5698-82) at day 5 to mark nuclei for dividing cells and quantified similarly to the live-dead stain using ImageJ.

In addition to the live/dead assay, a resazurin cell viability assay (Biotium, 30025) was performed on NIH/3T3s. Cells were allowed to adhere for 4h, then incubated in media containing 10% (v/v) resazurin. After 4h of incubation, 100μL of media per sample was transferred to a 96 well plate. The fluorescence was read using a microplate reader (ex./em. 560/590, BioTek Synergy 4). Cell-free scaffolds were also incubated in 10% resazurin and used as blanks to subtract any background fluorescence from the scaffolds. Media was changed and the assay repeated on days 1, 3, and 5 after initial cell attachment.

2.3.8 hPSC-CM differentiation and cell seeding

RUES2 hPSCs were expanded on Matrigel-coated 6-well plates (Corning, CLS354234) in mTeSR 1 media (Stemcell Technologies, 85850) with daily changes. Cells were passaged at 85–90% confluency at 1:6 by incubating for 4min in Versene (Gibco, 15040066), lifting with a cell scraper, and resuspending in media supplemented with 5μM Y-27632 dihydrochloride (LC Laboratories, Y-5301). To produce hPSC-CMs, the GiWi cardiac differentiation protocol was employed[80].

After 50 days of cardiac differentiation, the resulting hPSC-CMs were seeded on 8% PVA scaffolds containing 0%, low (3.25%), and high (9.75%) concentrations of PEDOT:PSS suspended on 18mm coverslips as well 0.1% gelatin-coated glass 18mm coverslips in 12-well plates. hPSC-CMs were dissociated in 0.5mL collagenase IV (4 mg/mL, Gibco, 17104-019) for 50min at 37 °C, followed by 25min in 0.5mL 0.25% Trypsin-EDTA (Gibco, 25200) at 37 °C. Cells were quenched in RPMI + B27 with insulin +20% FBS (v/v) + 5μM Y-27632 dihydrochloride and centrifuged at 400g for 10min. hPSC-CMs were resuspended in the quenching media and seeded at 10^4 (sub-confluent monolayer) or 10^6 (monolayer) cells per well (4×10^3 or 4×10^5 cells/cm^2, respectively).

2.3.9 RNA isolation, sequencing and analysis

hPSC-CMs on 8% PVA or conductive scaffolds were dissociated with 0.5mL 0.25% Trypsin-EDTA and pelleted centrifugation at 400*g* for 5min. The cells were resuspended in DPBS, re-pelleted, and lysed with 1mL QIAzol (Qiagen, 79306) for 5min. Chloroform was added 1:5 to QIAzol, shaken for 15s, and incubated for 3min. The samples were centrifuged for 10min at 15,000 RPM and 4 °C (Eppendorf, Centrifuge 5452 R) and the aqueous phase containing the RNA was transferred to new tubes. An equal volume of isopropanol was added, and the samples were allowed to rest for 10min, followed by a 10-min centrifugation at 15,000 RPM at 4 °C. The

supernatant was then removed and the RNA pellet was resuspended in 1mL of cold 75% molecular grade ethanol in diethylpyrocarbonate (DEPC) water. The samples were re-pelleted at 15,000 RPM at 4 °C, decanted, and resuspended in 100μL of DEPC water. An RNeasy Mini kit (Qiagen, 74104) was used to purify the RNA following the manufacturer's protocol. The final RNA concentration was measured by a Nanodrop spectrophotometer and the samples were stored at −80 °C for further processing.

Bulk RNA sequencing was performed by the Institute for Genomic Medicine at UC San Diego. Total RNA integrity was assessed via an Agilent TapeStation 4200. Samples with an RNA Integrity Number (RIN) above 8.0 were prepared using the Illumina Total RNA Prep (Ribodepletion) and sequenced with the Illumina NovaSeq 6000 with paired end reads (PE100). Quality of sequencing data was assessed using FASTQC[81]. Reads were aligned to the human reference genome hg38 using STAR[82] and gene counts were determined using featureCounts[83]. Log_2 fold changes of differentially expressed genes (DEGs) were determined with DESeq2[84] via a paired model of non-conductive versus conductive substrates and including biological replicates as a covariate. Top DEGs were filtered with a log_2 fold change greater than or equal to 0.25 and p-value less than or equal to 0.05 and used to construct a volcano plot via EnhancedVolcano[85], an MA plot via ggpubr's 'ggmaplot' function[86], as well as to determine gene ontology(GO) terms via g:Profiler[87]. For generating a principal component analysis (PCA) plot and heatmap, normalization of sequencing data into log_2 counts per million (cpm) was performed with edgeR[88]. Batch effect corrections due to biological replicates was performed with the sva package's 'ComBat' function[89] after averaging technical replicates. Normalized data with batch correction were used to generate a PCA plot via ggplot[90] and heat map via pheatmap[91]. Raw RNA-sequencing was deposited and is accessible in NCBI under the Gene Omnibus Express number GSE226541.

2.3.10 hPSC-CM immunofluorescent assays

After 50–70 days in culture, hPSC-CMs were allowed to adhere to conductive electrospun scaffolds and a glass control for 3 days prior to fixation with 3.7% paraformaldehyde (Fisher Scientific, O4042-500) in DPBS with calcium and magnesium (Corning, 20-030-CV) for 15min at room temperature. Cells were permeabilized in 0.5% (v/v) Triton X-100 (Fisher Bioreagents, BP151-100) for 10min and blocked for 1h in DPBS with calcium and magnesium containing 2% (w/v) bovine serum albumin (BSA, Goldbio, A-420-10) and 0.1% (v/v) Triton X-100. hPSC-CMs were incubated in either desmoplakin 1/2 (DP) (1:200, Biorad, 2722–5204) primary antibodies to determine cell-cell mechanical coupling, or α-actinin (1:800, Sigma-Aldrich, A7811) primary antibodies for detecting sarcomere organization for 2h at room temperature in the blocking buffer. Samples were then incubated in AlexaFluor 488 conjugated donkey anti-mouse (1:1000, Invitrogen, A21202) antibody and rhodamine-phalloidin (1:500, Biotium, 00027) for 2h at room temperature. Samples were finally incubated in Hoechst 33342 in DI water (1:2000, Invitrogen, H3570) for 15min at room temperature, mounted on slides with Fluoromount-G (Southern Biotech, 0100-01), and allowed to dry overnight prior to immunofluorescent (IF) imaging. A Zeiss LSM 780 confocal microscope with a 63× oil objective and Nikon Eclipse Ti microscope with a Yokogawa CSU-X1 confocal attachment and a 60× water objective were used to image DP and α-actinin.

DP intensity analysis was performed with ImageJ with brightness and contrast adjusted to overexpose the area of the image with cells and then converted to an inverted binary image. The mask was applied to the original DP channel such that the mean pixel intensity was only quantified in the region of the image with hPSC-CMs. For sarcomere organization, images were converted into 8-bit, split into individual channels, and the background was removed from the α-actinin

channel. A grid was placed over the image and a random number generator was used to select regions of interest for analysis. Each region was analyzed using an open-source MATLAB script[92] that produces a normalized organization index.

2.3.11 Calcium handling

hPSC-CMs were seeded at sub-monolayer and monolayer densities on electrospun scaffolds with increasing PEDOT:PSS concentration. hPSC-CMs were further seeded on 0.1% gelatin coated 35mm glass bottom culture dishes. After 3 days of attachment, scaffolds were transferred to 35mm glass bottom culture dishes and incubated with 2μM fluo-4 AM ester (Biotium, 50018) in RPMI + B27 with insulin for 15 minutes at 37 ºC in the dark. After 15 minutes, the scaffolds were inverted in the dish and imaged using a Nikon Eclipse Ti microscope with a Yokogawa CSU-X1 confocal attachment and a 60x water objective. Five videos per sample across 3-4 biological replicates were captured for 30 seconds with 100ms intervals for a total of 301 frames. In ImageJ, the rotated rectangle tool was used to select 1-pixel wide sections perpendicular to the calcium flux on individual cells. The selection was duplicated and converted into an orthogonal XZ view. Two sections per cell were analyzed. The XZ projections were saved and analyzed using a custom MATLAB script, which is available via Github (https://github.com/englea52/PEDOT_PSS).

2.3.12 FluoVolt imaging

hPSC-CMs were seeded at monolayer densities on electrospun scaffolds with increasing PEDOT:PSS concentration and gelatin-coated glass. After 7 days of attachment, scaffolds were incubated in FluoVolt membrane potential dye (Invitrogen, F10488) in Tyrode's solution (Thermo Scientific Chemicals, J67593-K2) following the manufacturer's protocol. Briefly, scaffolds were washed twice with Tyrode's solution and incubated with FluoVolt loading solution at 37 ºC in the

dark. Scaffolds were then washed twice in Tyrode's solution, inverted onto a glass bottom well plate (Cellvis, P24-0-N), and maintained in fresh Tyrode's solution for imaging. Samples were imaged on an Andor Dragonfly spinning disk confocal microscope. Five videos per sample across 3 biological replicates were captured for 20 seconds with 2.5ms intervals. In ImageJ, the rotated rectangle tool was used to select 1-pixel wide sections across several regions of interest (ROIs) in each video (5 ROIs per monolayer or 1 ROI per cell cluster in instances lacking a monolayer). ROIs were analyzed similarly to calcium handling sections using our custom MATLAB script.

2.3.13 Statistical analysis

The respective statistical tests and n numbers are described in the figure legends. The following statistical significance cut off was applied: $p > 0.05$, *$p < 0.05$, **$p < 0.01$, ***$p < 0.01$, ****$p < 0.0001$. Data expressed as box-and-whisker plots show all points with the whisker ends corresponding to minimum and maximum values. All other values are expressed as mean ± SD. Statistical analyses were performed using GraphPad Prism Software v9.0.

2.4 Results and discussion

2.4.1 Characterization of PEDOT:PSS/PVA electrospun scaffolds

To create fibrillar conductive scaffolds, we blended and electrospun PVA and PEDOT:PSS and crosslinked the resultant scaffolds for either 15 or 30 minutes to prevent PVA dissolution in solution (Figure 2.1, a-b). PVA scaffolds remained fibrous for up to 4 weeks in solution with 30-minutes of crosslinking, although the addition of 9.75% PEDOT:PSS to the same scaffold (Figure 2.1, c) led to an initial increase in fiber diameter compared to PVA-only scaffolds (Figure 2.1, d). However, conductive fiber diameters remained within the range of fiber diameters within collagen type I gels[93]. Since PVA scaffolds crosslinked at 30 minutes experienced the least amount of fiber annealing over time, subsequent experiments were performed on these scaffolds.

Along with scaffold structure, material stiffness is well-known to affect stem cell fate and cell spreading[94,95]; hence, we also assessed electrospun scaffolds stiffness. Bulk stiffness scaled with PEDOT:PSS concentration (Figure 2.1, e) and stiffness values spanned a range consistent with normal cardiac muscle[96] . The large variance observed in stiffness values may reflect the random nature of the PVA mesh from electrospinning, despite using larger AFM probes for measurement. Since hPSC-CMs are electrically active cells and given the anisotropic structure of electrospun scaffolds[97], we measured PEDOT:PSS/PVA scaffold conductivity using TLM, which uses a network of variable length resistors made by the scaffolds to evaluate contact resistance and sheet resistance[78,79] (Supplemental Figure 2.1). 8% PVA was non-conductive, i.e., insulating, whereas conductivity increased substantially with PEDOT:PSS concentration, up to 7 x 10^{-3} S/cm^2 (Figure 2.1, f). These data suggest scaffold properties are consistent and mimic physiologically relevant conditions when crosslinked at 30 minutes and additional electrically conductive properties are achievable with the incorporation of PEDOT:PSS.

2.4.2 PEDOT:PSS/PVA biocompatibility

To ensure that hPSC-CM results were not affected by variable attachment, proliferation, or survival, we first determined how a non-conductive cell type, e.g., NIH/3T3 fibroblasts, behaved on the electrospun scaffolds. Cells preferentially adhered to conductive scaffolds and glass versus non-conductive scaffolds (Figure 2.2, a-c) but remained >90% viable on all substrates. Given that 8% PVA scaffolds are thinner due to their lower total polymer mass compared to our highest PEDOT:PSS percentage of 9.75%, we introduced an 11% PVA scaffold as a mass-matched control to the 9.75% condition. Independent of mass, however, cell attachment remained higher on conductive scaffolds compared to both non-conductive controls (Figure 2.2, d). To quantitatively assess proliferation, we also monitored metabolic changes over five days by resazurin reduction.

Given higher initial cell attachment on the conductive scaffolds compared to PVA-only scaffolds (Figure 2.2, a-c), fluorescence intensity signal was greater on conductive scaffolds at day 0 and remained higher on conductive scaffold over the time course (Figure 2.2, e). Gelatin-coated glass had the highest attachment, perhaps due to the presence of ECM proteins, which were purposefully excluded from the electrospun scaffold samples to directly assess cell adhesion to the fiber and not a matrix coating. Yet, serum proteins are classically known to deposit on electrically conductive substrates[98], hence the enhanced cell binding to PEDOT:PSS versus PVA could be due to non-specific serum protein binding. Resazurin reduction is affected by initial adhesion, hence we also stained cells for the proliferation marker Ki67, which enables single cell assessment of proliferation. While we found differences with cells cultured on gelatin-coated glass, there were no differences in proliferation between scaffolds of varying PVA and PEDOT:PSS (Figure 2.2, f). Similarly high levels of cell adhesion and proliferation to PEDOT:PSS fibers and substrates have been reported with other mouse and human fibroblast lines relative to control fibers or surfaces[99,100], suggesting that conductive substrates have low cytotoxicity and support cell adhesion and proliferation.

2.4.3 Conductive scaffolds upregulate cardiac-related genes, improve cytoskeletal structures, and aid calcium handling and membrane depolarization

Given their compatibility, we next determined how conductive scaffolds generate transcriptomic differences within hPSC-CMs. Principal component analysis (PCA) (Figure 2.3, a; left) shows clustering due to substrate, while the Euclidean distance matrix illustrates the increased dissimilarity between conductive and non-conductive scaffolds (Figure 2.3, a; right). Using an adjusted p-value (p-adj.) value of less than 0.05 and log fold change (FC) cut-off of 0.25, 287 differentially expressed genes (DEGs) were identified between the hPSC-CMs seeded on the PVA-

only and PEDOT:PSS scaffolds (Figure 2.3, b). Gene ontology (GO) terms associated with PVA-only scaffolds included response to external stimulus, immune system process, response to virus, and innate immune response, illustrating an increased stress response on PVA-only scaffolds. In contrast, the presence of PEDOT:PSS produced terms related to heart contraction, heart process, muscle system process, muscle contraction, and a decreased stress response (Figure 2.3, c). We further plotted the normalized gene expression of cardiac genes related to these GO terms and found hPSC-CM contractility (*MYH6, MYH7, MYL7*), sarcomere organization (*TCAP*), and electrophysiology (*KCNIP2, ATP1A2, RNF207*) gene expression was elevated on conductive scaffolds (Figure 2.3, d). Given that *MYH7* is a marker of hPSC-CM maturity[101], these findings suggest that a conductive environment not only leads to increased contractility gene expression but may also result in additional maturation beyond protocols used to differentiate hPSC-CMs initially[80]. While the switch from *MYL7* to *MYL2* is another marker of maturity[101], *MYL2*, though not a DEG, has higher expression on hPSC-CMs on conductive scaffolds compared to PVA-only scaffolds (Supplemental Table 2.1). Our results also indicated the upregulation of *TCAP,* which encodes for titin-cap and enables titin assembly at the Z-disk[102], as well as electrophysiological genes on PEDOT:PSS/PVA scaffolds. Based on our transcriptomic analysis, we find that PEDOT:PSS/PVA scaffolds cause increased contractility, sarcomere, and electrophysiological gene expression, which may impact hPSC-CM function.

To assess the morphological and functional impact of the transcriptomic differences, we first looked at desmoplakin, which provides cardiac mechanical stability and aids in electrical communication through the maintenance of gap junctions[103,104]. After 3 days of exposure to experimental substrates, DP was highly localized to the hPSC-CM perimeters on conductive scaffolds compared to non-conductive scaffolds (Figure 2.4, a). Mean DP fluorescence intensity

was similar between gelatin-coated glass and conductive scaffolds, indicating that similar DP expression for mechanical stability can be achieved on electrospun scaffolds even in the absence of native ECM components (Figure 2.4, b). Further, the differences between conductive and non-conductive scaffolds were statistically significant, illustrating that a conductive microenvironment aids in mechanical stability. In addition to DP, organized sarcomeres are necessary for the contractility of hPSC-CMs[105]. hPSC-CMs were seeded at either 10^4 (sub-confluent monolayer) or 10^6 (monolayer) cells ($4x10^3$ or $4x10^5$ cells/cm^2, respectively) per condition to determine if the conductive scaffolds could promote sarcomere organization in hPSC-CMs that are not directly in contact with one another. At both seeding densities, scaffolds containing PEDOT:PSS improved sarcomere organization index compared to PVA-only (Figure 2.4, c), when assessed via an unbiased organization index, which scaled with increasing PEDOT:PSS concentration even in the absence of a confluent monolayer (Figure 2.4, d); sarcomere organization differences were also indicative in overall morphology differences as a function of increasing PEDOT:PSS concentration (Supplemental Figure 2.2) and were not impacted by differences in CM purity between substrates (Supplemental Figure 2.3). These results suggest that the presence of PEDOT:PSS permits sarcomeres to organize in hPSC-CMs with or without a monolayer and integrin attachment points, further establishing the importance of a conductive scaffold for electrical signal propagation.

Intracellular calcium homeostasis involves the release and reuptake of calcium through various calcium handling machinery, resulting in subsequent contractions and force generation by sarcomeres[106,107]. Intercellular calcium, and therefore cell-cell electrical communication, is facilitated by gap junctions and allows for synchronous contractions of hPSC-CMs[108]. Thus, we investigated functional maturity through assessment of calcium handling kymographs in either the

absence or presence of a confluent monolayer (Figure 2.5, a). For both cell densities, conductive scaffolds had more intense and frequent calcium spikes relative to 8% PVA-only scaffolds (Figure 2.5, b); normalized fluorescent intensity (dF/F_0) was highest in the presence of PEDOT:PSS at both cell densities compared to all other substrates (Figure 2.5, c). This suggests that the presence of PEDOT:PSS allows for a larger calcium flux from the sarcoplasmic reticulum (SR) into the cytoplasm of hPSC-CMs[109], implying stronger contractions. In addition to dF/F_0, the time for each calcium cycle to peak decreased at both low and high seeding densities on PEDOT:PSS compared to PVA-only scaffolds (Figure 2.5, d), demonstrating that conductive scaffolds enable rapid calcium efflux. Although cycle length and width (Figure 2.5, e-f), which indicate how fast calcium is being taken into the SR, did not decrease with increasing PEDOT:PSS concentration in non-monolayer cells , both values decreased in the presence of a monolayer. Likewise, when comparing cycle length and width, there was density-dependent improvement in timing of hPSC-CMs seeded on the same substrate (Figure 2.5, e-f). Thus, signal intensity is enhanced by conductivity through the presence of PEDOT:PSS whereas signal timing is enhanced by monolayer confluence.

To further probe the effect of conductive substrates on the cell retention and electrophysiology of hPSC-CMs over an extended period, i.e. 7 days of culture, we assessed action potential intensities and depolarization events of these cells seeded in monolayer on our substrates. After 7 days of culture, hPSC-CMs failed to form monolayers on 8% PVA (Figure 2.6, a), while monolayers were maintained on all other conditions. Assessed kymographs (Figure 2.6, b) illustrate how decreased cell attachment on 8% PVA resulted in asynchronous depolarization events, while the enhanced attachment to conductive scaffolds allowed for synchronicity across independent ROIs. Further, overall action potential intensity remained significantly higher on conductive substrates (Figure 2.6, c), similar to calcium flux experiments (Figure 2.5, c) performed

after only 3 days of culture. This suggests that over time, the electrophysiological function, particularly signal intensity, remains higher across hPSC-CMs in the presence of PEDOT:PSS, and it may be supported through voltage-gated sodium channels such as Nav1.5 which is responsible for initial membrane depolarization[110]. Interestingly, the total percentage of depolarizing ROIs decreased on non-conductive substrates, i.e. glass and 8% PVA scaffolds, compared to PEDOT:PSS scaffolds (Figure 2.6, d). Therefore, while cells experienced improved attachment to gelatin-coated glass compared to 8% PVA, they experienced an almost identical percentage of depolarizing events, likely due to the lack of a conductive microenvironment to assist in signal propagation. Because of these differences in depolarization events, temporal parameters such as cycle length became difficult to interpret across different substrates. While 8% PVA had similar cycle length to 9.75% PEDOT:PSS scaffolds, the lower percentage of depolarizing ROIs and lack of monolayer made these comparison difficult as cell density affects action potentials in hPSC-CMs[111]. However as a function of PEDOT:PSS, cycle length decreased such that cells depolarized more often on 9.75% PEDOT:PSS scaffolds. Taken together with calcium handling, these data demonstrate that PEDOT:PSS allows for higher calcium and action potential intensity as well as synchronicity in hPSC-CMs, both of which are illustrative of improved electrical maturity.

2.5 Conclusion

Here we constructed composite PEDOT:PSS/PVA electrospun scaffolds to enhance the structural and functional maturity of hPSC-CMs in the absence of external stimuli. These scaffolds are biocompatible, capable of mimicking mechanical and physical properties of native cardiac tissue and provide a conductive microenvironment for electrical signal propagation. Initial transcriptomic analysis revealed upregulated cardiac genes in hPSC-CMs on conductive scaffolds,

motivating further investigation of important structural protein organization and functionality. We found an increase in DP localization and sarcomere organization of hPSC-CMs in the conductive environment compared to an insulating (non-conductive) environment and, surprisingly, saw that sarcomere organization increased under these conditions even in the absence of a cell monolayer. Calcium handling experiments further revealed improved functional maturity of both low and high density hPSC-CMs on conductive scaffolds, indicated by increased calcium signal intensity and decreased time to peak. Upon investigating how these cells responded to PEDOT:PSS after a prolonged time in culture, we found improved cell retention, higher instances of depolarizing ROIs, and stronger action potential intensities on conductive substrates. While many groups have investigated the effects of conductive materials in hPSC-CM maturity, including the use of PEDOT:PSS[112], here, we have demonstrated that maturity can be achieved in the absence of external stimulation or a confluent monolayer if hPSC-CMs are provided with a conductive microenvironment. Taken together, these data suggest that conductive polymer platforms are capable of conducting electrical signals between distant hPSC-CMs, further warranting their investigation in 3D engineered tissue constructs or for application in disease modeling purposes.

2.6 Figures

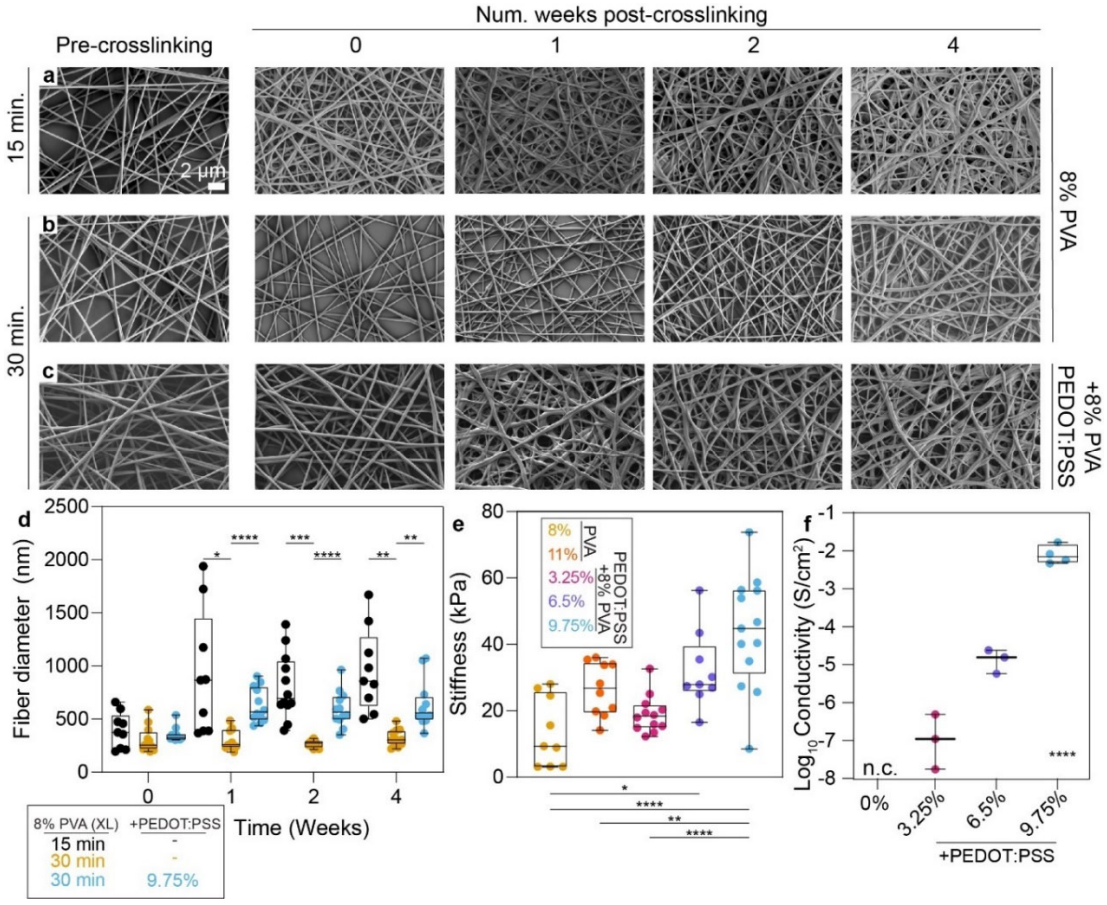


Figure 2.1: Physical characterization of electrospun scaffolds.

(a) SEM images of 8% PVA electrospun scaffolds incubated in DPBS 4 weeks post-crosslinking with glutaraldehyde vapor for 15 minutes, (b) 30 minutes, and (c) 30 minutes with 9.75% PEDOT:PSS/PVA. Scale bar = 2 µm. (d) After 4 weeks of incubation, 8% PVA crosslinked (XL) for 15 minutes had a median fiber diameter of 828.04 nm (n = 3 scaffolds for week 0, 1, 4; n = 4 scaffolds for week 2; 3 average measurements per scaffold), while 8% PVA crosslinked for 30 minutes had a median fiber diameter of 302.7 nm and 560.1 nm with PEDOT:PSS (n = 4 scaffolds per timepoint, 3 average measurements per scaffold). (e) Bulk stiffness (kPa) of PVA-only (8% and 11%) and 8% PVA with PEDOT:PSS (3.25%, 6.5%, and 9.75% mass ratio) electrospun scaffolds crosslinked for 30 minutes measured by AFM. Median stiffness values of 8% PVA, 11% PVA, 3.25%, 6.5%, and 9.75% were 9.30, 26.68, 18.36, 27.91, and 44.76 kPa, respectively (n = 4 scaffolds per condition; 1 point represents 1 force map). (f) Conductivity measurements of 8% PVA electrospun scaffolds containing 0 – 9.75% PEDOT:PSS measured by TLM. Median conductivity values of 3.25%, 6.5%, and 9.75% were 1.09×10^{-7}, 1.57×10^{-5}, and 7.00×10^{-3} S/cm^2, respectively. Each point indicates one scaffold (n.c. indicates not conductive, n = 2). Statistical significance was determined via a mixed-effects analysis (d), a one-way ANOVA with Tukey's multiple comparison test (e), or just a one-way ANOVA (f).

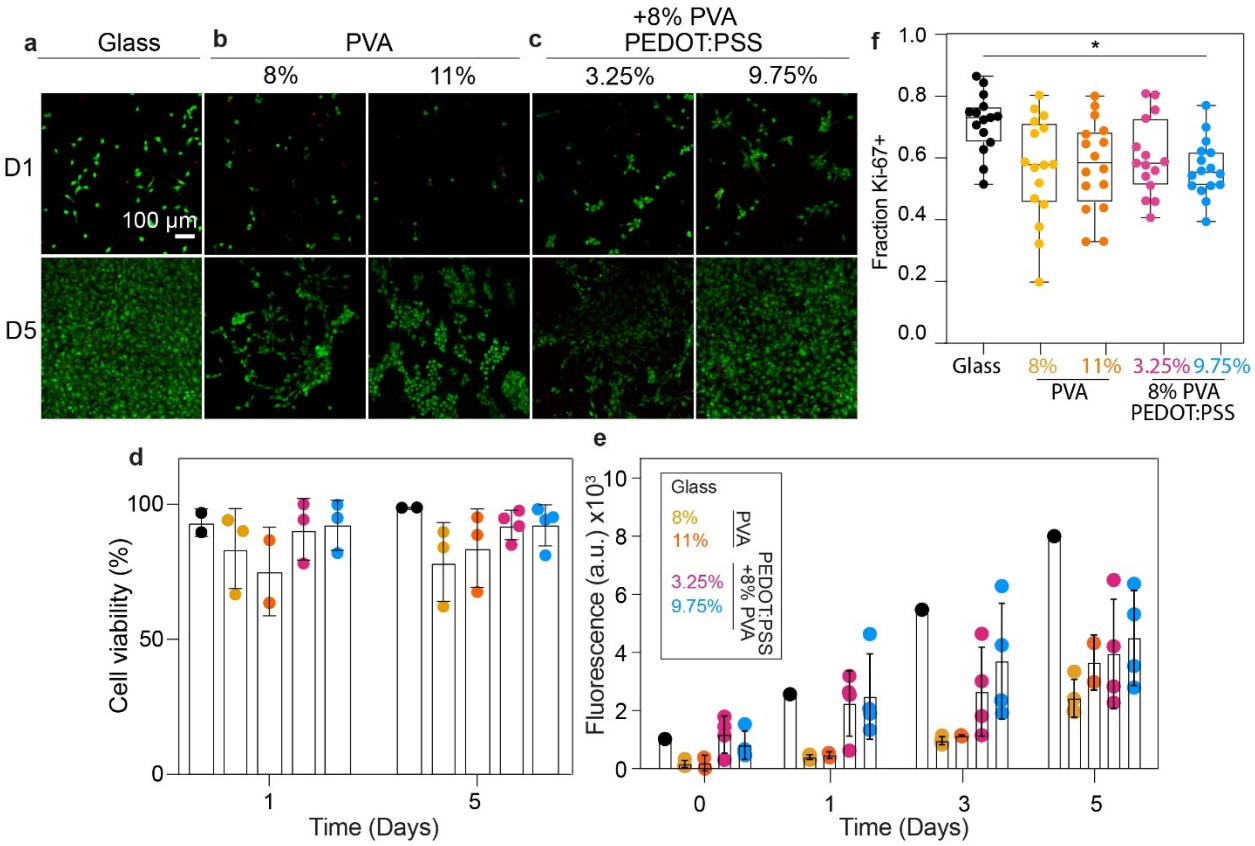


Figure 2.2: Cells are viable and proliferative independent of PEDOT:PSS concentration.

LIVE/DEAD staining 1 and 5 days after NIH/3T3 cell seeding on (a) glass, (b) 8% and 11% PVA, and (c) 8% PVA scaffolds containing 3.25% and 9.75% PEDOT:PSS. Green indicates live cells and red indicates dead cells. Scale bars (a-c) = 100 µm. (d) Cell viability was calculated as the number of live cells over the total (live + dead) cells and represented as mean ± std dev. At day 5, cell viability is above 90% for glass and electrospun scaffolds containing PEDOT:PSS. For D1, n = 2, 3, 2, 3, and 3 for glass, 8% and 11% PVA, and 8% PVA scaffolds containing 3.25% and 9.75% PEDOT:PSS, respectively. For D5, n = 2, 3, 3, 4, and 4 for glass, 8% and 11% PVA, and 8% PVA scaffolds containing 3.25% and 9.75% PEDOT:PSS, respectively. (e) Cell proliferation (mean ± std) as measured by resazurin fluorescence intensity illustrates higher cell viability with increasing PEDOT:PSS concentration as compared to PVA-only scaffolds. For D1, n = 1, 4, 2, 4, and 4 for glass, 8% and 11% PVA, and 8% PVA scaffolds containing 3.25% and 9.75% PEDOT:PSS, respectively. For D5, n = 1, 4, 2, 4, and 4 for glass, 8% and 11% PVA, and 8% PVA scaffolds containing 3.25% and 9.75% PEDOT:PSS, respectively. (f) The fraction of Ki67 positive cells is indicated in the plot at day 5 post-plating on the indicated scaffolds. Statistical significance was determined via a mixed-effects analysis for (d), a two-way ANOVA for (e), or a one-way ANOVA for (f), both with Tukey's multiple comparison test.

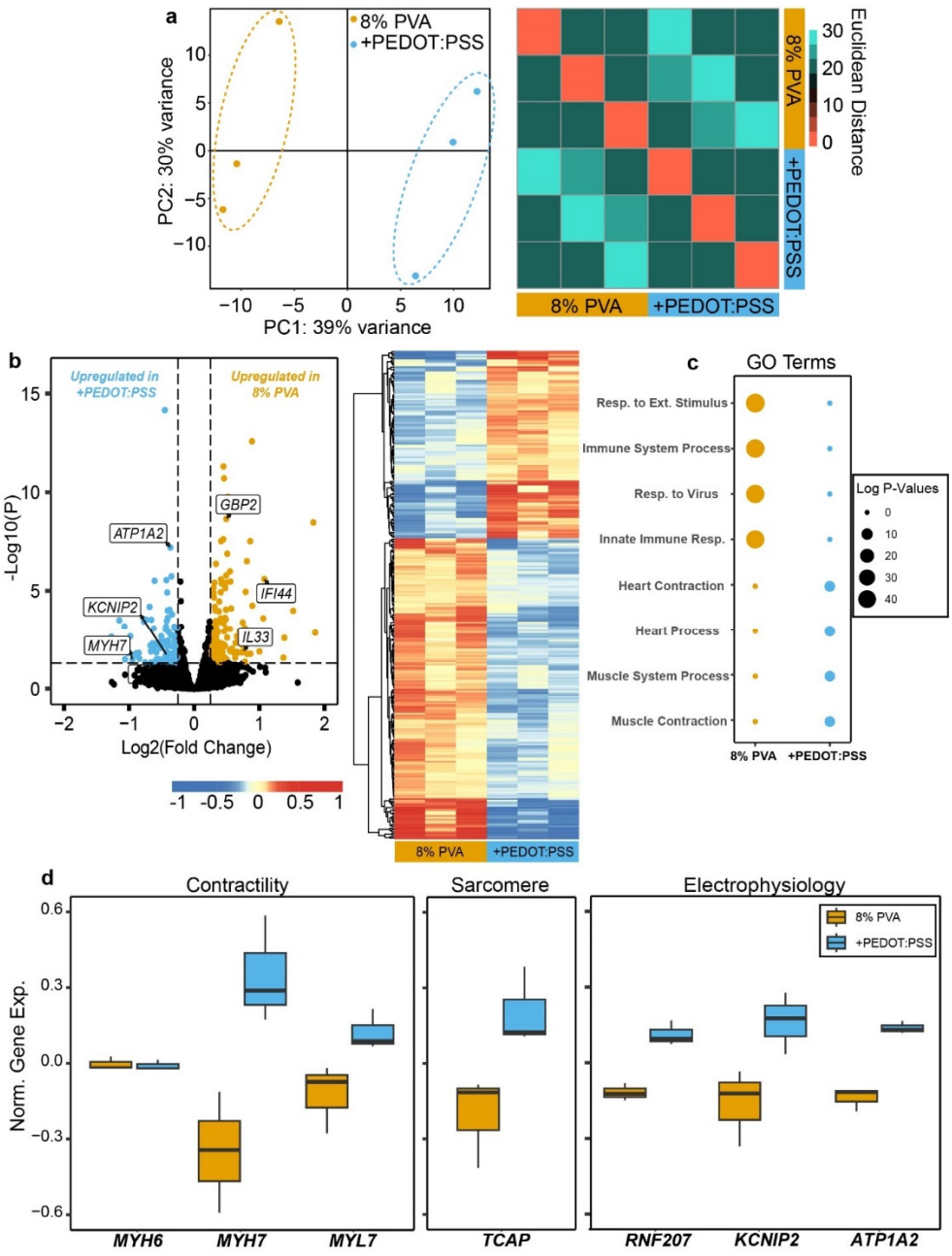


Figure 2.3: RNA sequencing identifies upregulation of cardiac-related genes on conductive substrates.

(a) PCA (post-batch correction) for hPSC-CMs seeded on 8% PVA or 8% PVA+9.75% PEDOT:PSS scaffolds with total contribution from each axis noted (left) and Euclidian distance matrix (right) indicating the similarity between groups, where 30 indicates the largest dissimilarity between samples. (b) Volcano plot (left) indicating differences in DEGs between 8% PVA and conductive scaffolds and heatmap (right) illustrating transcriptomic clustering of the top 287 significant genes. (c) Top four GO terms for each experimental condition and their statistical significance. (d) Normalized expression of genes related to hPSC-CM contractility, sarcomere organization, and electrophysiology (p-adj. < 0.05). A FC cut-off > 0.25 and p-adj. cut-off < 0.05 for (b) and (c) was used.

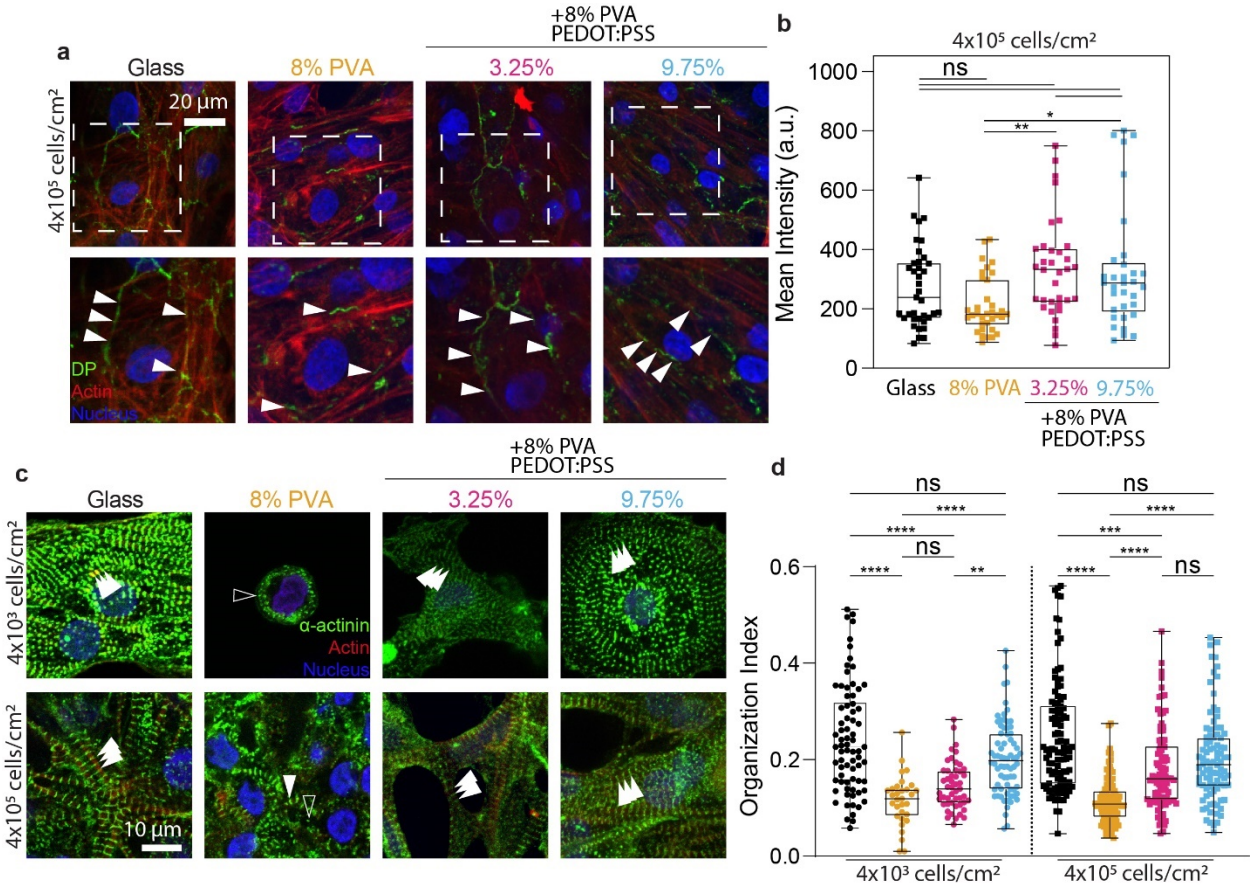


Figure 2.4: Structural characterization of hPSC-CMs.

(a) IF images of desmoplakin (DP) localization in hPSC-CMs seeded on glass, 8% PVA, and PEDOT:PSS/PVA (3.25% and 9.75%) electrospun scaffolds at 10^6 cells per condition. Scale bar = 20 µm. (b) Mean DP pixel intensity is plotted for each condition. Data is reported as the mean pixel intensity of desmoplakin across four biological replicates with 5-11 images per sample. (c) IF images of hPSC-CMs seeded on glass, 8% PVA, and PEDOT:PSS/PVA (3.25% and 9.75%) electrospun scaffolds at 10^4 and 10^6 cells per 18 mm coverslip. Filled arrowheads indicate organized sarcomeres and open arrowheads indicate unorganized sarcomeres. Scale bar = 10 µm. (d) Sarcomere organization index is plotted for the indicated scaffold compositions on a scale of 0 (least) to 1 (most) organized. Each point represents one section of an image across three biological replicates. Statistical significance was determined via a one-way ANOVA with Tukey's multiple comparisons test (b) and Kruskal-Wallis test with Dunn's multiple comparisons (d) test to account for unequal variance between experimental groups.

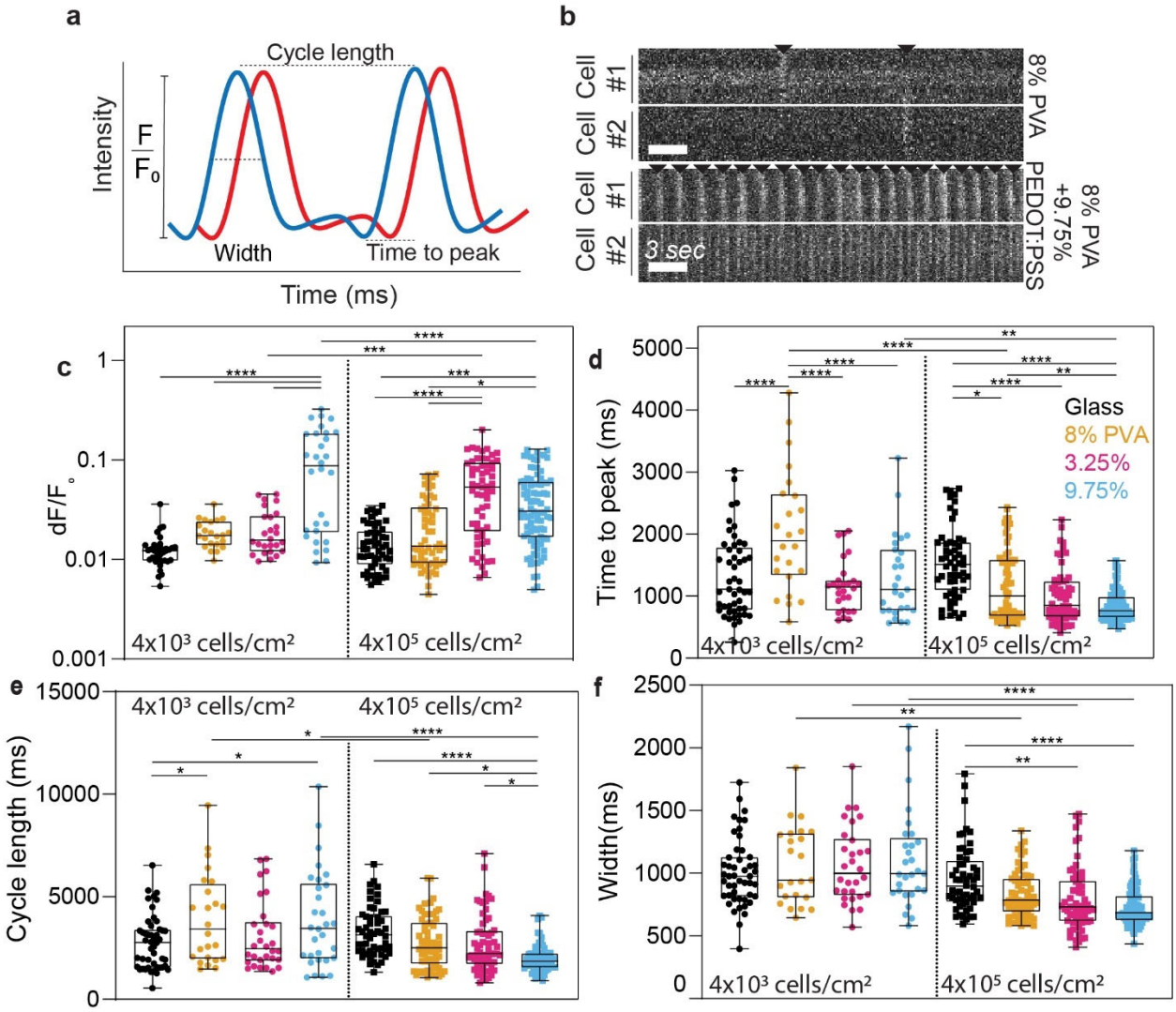


Figure 2.5: hPSC-CM calcium handling on conductive PEDOT:PSS/PVA electrospun scaffolds.

(a) Graphical illustration of relevant calcium handling parameters. (b) Kymograph of hPSC-CMs in monolayer on 8% PVA or 9.75% PEDOT:PSS/PVA. Black chevron indicates calcium peak. Scale = 3 seconds. dF/Fo (c) increases and time to peak (d) decreases with increasing PEDOT:PSS concentration in both low and high hPSC-CM seeding densities. Cycle length (e) and width (f) decrease with increasing PEDOT:PSS concentration at high seeding densities. Each point represents one cell across n = 3 biological replicates. Statistical significance was determined by one-way ANOVA with Tukey's multiple comparison test.

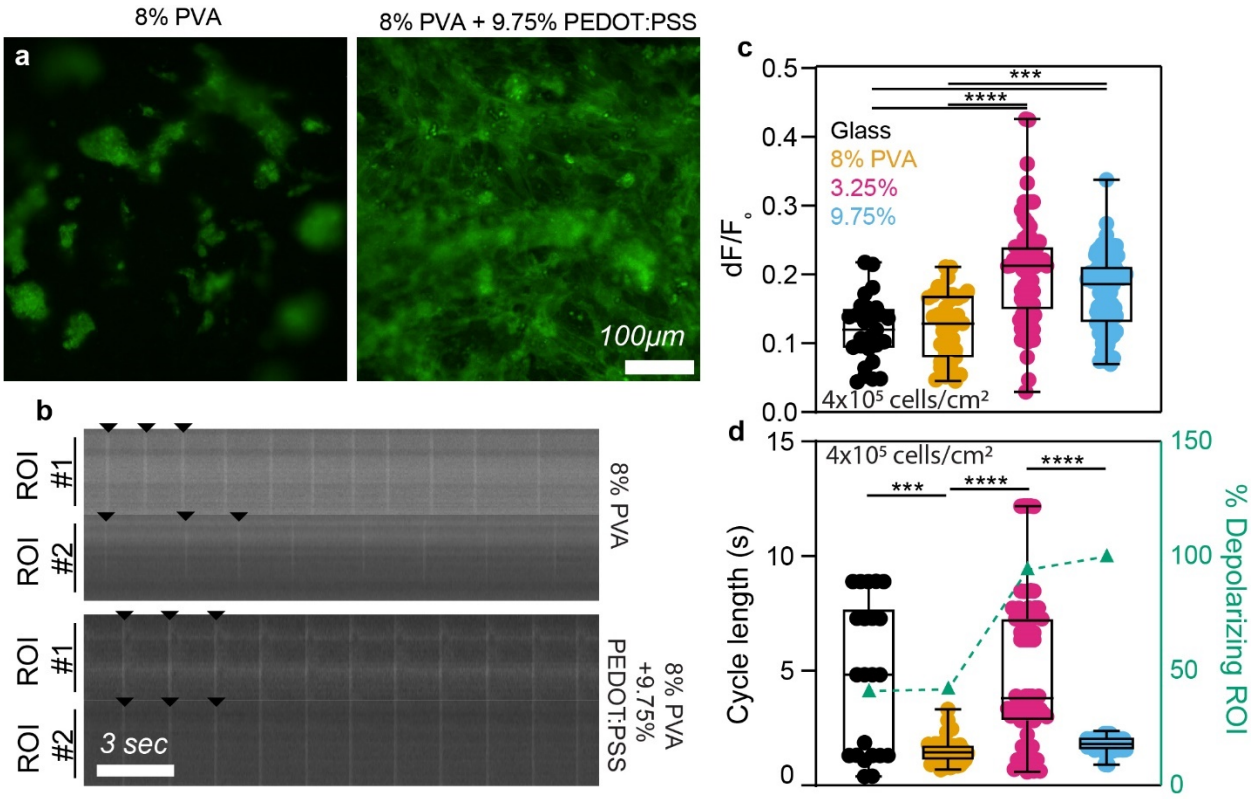
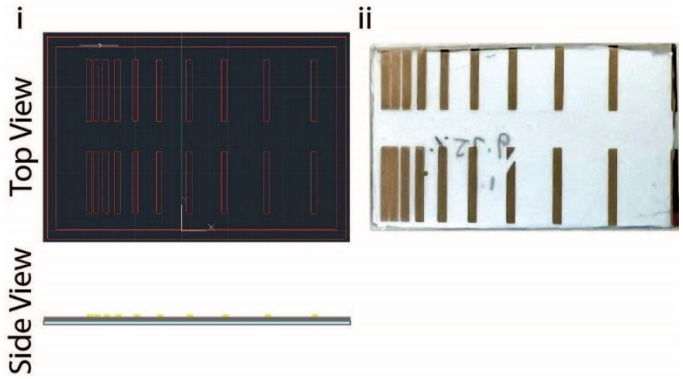


Figure 2.6: hPSC-CM action potentials on conductive PEDOT:PSS/PVA electrospun scaffolds.

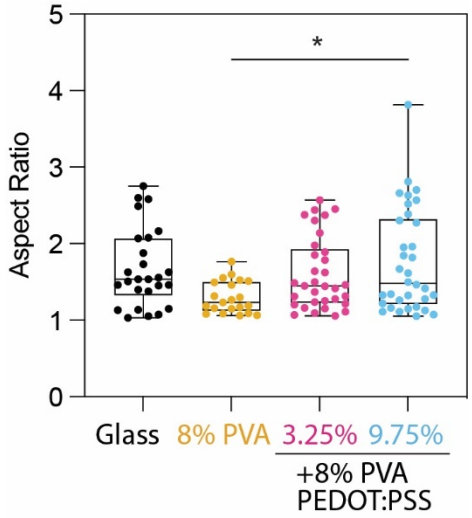
(a) Representative images of hPSC-CMs seeded in monolayer and stained with voltage sensitive dye FluoVolt after 7 days of culture on 8% PVA or 9.75% PEDOT:PSS/PVA. Scale = 100 μm (b) Kymograph of hPSC-CMs ROIs on 8% PVA or 9.75% PEDOT:PSS/PVA. Black chevron indicates action potential peak. Scale = 3 seconds. (c) dF/Fo was measured on conductive scaffolds and plotted relative to glass and 8% PVA. (d) Cycle length for rhythmically contracting cells was measured from kymographs and plotted. Since not all samples were rhythmically contracting, total percentage of depolarizing ROIs was also plotted (green) with the most number of depolarizing ROIs on conductive scaffolds (glass = 41.2%; 8% PVA = 42.3%; 3.25% = 94.4%; 9.75% = 100%). Each point represents one ROI across n = 3 biological replicates. Statistical significance was determined by Kruskal-Wallis test with Dunn's multiple comparison test.

2.7 Supplemental figures



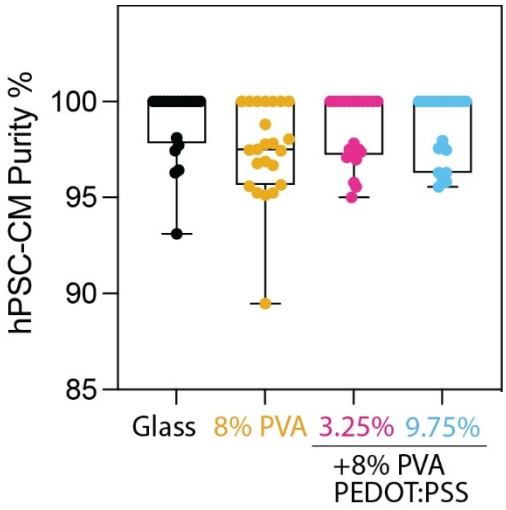
Supplemental Figure 2.1: Experimental setup for TLM measurements on electrospun scaffolds.

Top view: Autodesk AUTOCAD mask (i) designed to create a hard mask for metal deposition on electrospun scaffolds as seen in (ii). Side view: glass coverslip (bottom) with electrospun scaffold (middle) and gold contacts (top) for final TLM measurements. Patterns are 1 cm wide with inter-contact spacings of 500, 1000, 2000, 3000, 4000 and 5000 μm.



Supplemental Figure 2.2: hPSC-CM morphology.

Plot of CM major to minor axis as measured from α-actinin immunofluorescent images at 10^4 cells per scaffold. Statistical significance was determined by one-way ANOVA with Tukey's multiple comparison test with *$p<0.05$.



Supplemental Figure 2.3: hPSC-CM purity.

Plot of the percentage of cell expressions α-actinin via immunofluorescent images at 10^4 cells per scaffold. Statistical significance was determined by one-way ANOVA with Tukey's multiple comparison test with *$p<0.05$.

2.8 Acknowledgements

Chapter 2, in full, is a reprint of the material as it appears in Biomaterials. Gonzalez G, Nelson AC, Holman AR, Whitehead AJ, LaMontagne E, Lian R, Vatsyayan R, Dayeh SA, & Engler AJ. Conductive electrospun polymer improves stem cell-derived cardiomyocyte function and maturation. Biomaterials. 2023;302:122363. doi:10.1016/j.biomaterials.2023.122363. The dissertation author was the primary investigator and author of this paper.

The authors would like to thank Dr. Neil Chi (UCSD) for the donation of the RUES2 ESCs, Dr. Karen Christman (UCSD) for access to the BioTek plate reader, Dr. Kristen Jepsen of the Institute for Genomic Medicine (UCSD) for technical assistance with sequencing, Dr. Elsa Molina (Sanford Consortium Stem Cell Core) for access and maintenance of the LSM 780 microscope, and Dr. Max Rempel (Sanford Consortium Stem Cell Core) for access and maintenance of the Andor Dragonfly microscope. This work was performed in part at the San Diego Nanotechnology Infrastructure (SDNI) of UCSD, a member of the National Technology Coordinated Infrastructure (NNCI), which is supported by the National Science Foundation (ECCS-2025752). The authors acknowledge funding and equipment support from the National Institutes of Health (R01AG045428 to A.J.E. and DP2EB029757-01 to S.A.D.). Fellowship support was provided by the American Heart Association (20PRE35180060 to A.C.N.), the National Science Foundation (to G.G., E.L., and A.J.W.), the San Diego Fellowship (to G.G.), and the National Institutes of Health (F31 HL163996 to A.R.H.).

Chapter 3 Conductive microfibers improve stem cell-derived cardiac spheroid maturation

3.1 Abstract

Given the prevalence of cardiovascular disease (CVD) worldwide and in the US, there is a need for mature cardiac models that recapitulate the disease complexity and function of native cardiac tissue. Conventional two-dimensional (2D) human pluripotent stem cell-derived cardiomyocytes (hPSC-CMs) differentiations fail to achieve the maturity levels of more intricate three-dimensional (3D) cardiac models. Given their high throughput qualities, cardiac spheroids are attractive models that have demonstrated improved functional and transcriptional maturity over conventional 2D differentiations. However, cardiac spheroid models fail to reach the maturity of more complex engineered cardiac tissues with lower throughput. Therefore, we explored how conductive polymer microfibers may be incorporated into hPSC-CM cardiac spheroids to accelerate their maturation compared to traditional 3D cardiac spheroids. By cryo-sectioning conductive electrospun polymer scaffolds, we created a library of conductive microfibers that could be readily incorporated into cardiac spheroids. Upon assessing the contractility of cardiac spheroids in the absence or presence of non-conductive or conductive microfibers, we found that conductive microfiber cardiac spheroids experienced improved contractility parameters over time. Further, the presence of conductive microfibers resulted in spheroids with a thicker ring-like perimeter and less compacted cavity, aiding in their contractility compared to control cardiac spheroids. Such functional improvements correlated with an increase in contractility and calcium handling-related cardiac proteins, as well as improved calcium handling abilities. Taken together, these data suggest that conductive microfibers can accelerate the maturity of traditional cardiac

spheroids while maintaining their high throughput quality to improve our ability to model cardiac diseases and target CVD.

3.2 Introduction

Cardiovascular disease (CVD) remains the leading cause of death worldwide, with nearly 1 million deaths per year in the United States alone[113]. Yet, despite this concerning figure, the total number of new clinically approved CVD therapies has trailed those for oncology and neurology, particularly due to the high cost of clinical trials and disease complexity[114,115]. To mitigate these issues, human pluripotent stem cell-derived cardiomyocytes (hPSC-CMs) have been extensively explored to serve as preclinical platforms for disease modeling and personalized drug screening as well as potential therapeutics for infarcted heart regions[1,2].

While two-dimensional (2D) hPSC-CM differentiations such as the GiWi protocol[116] have been widely applied, the resulting hPSC-CMs inherently lack the structural and functional complexity of three-dimensional (3D) constructs, resulting in an immature phenotype[101]. Therefore, there is a need for cardiac models that recapitulate the 3D cellular and extracellular matrix (ECM) interactions of the heart while maintaining a balance of tissue maturity and throughput[117]. Commonly explored 3D cardiac models range in intricacy from high throughput, self-assembled aggregates of cardiac spheroids and organoids[118] to highly engineered heart tissues (EHTs)[24] and 3D bio-printed scaffolds[62] with lower throughput. While cardiac spheroids allow for high throughput assays and demonstrate a shift towards mature adult cardiac tissue over 2D models[119], these constructs continue to lack the modularity and forces achievable through more complex, low throughput models. However, by manipulating the composition of cardiac spheroids with biomaterials to improve the electrical communication between hPSC-CMs, their functionality may be accelerated to achieve both high throughput and mature cardiac models.

Previously, we developed poly(vinyl alcohol) (PVA) biocompatible electrospun polymer constructs containing conductive poly(3,4-ethylenedioxythiophene) poly(styrene sulfonate) (PEDOT:PSS) and demonstrated they are viable sources for transcriptional, structural, and functional maturity of hPSC-CMs in 2D cultures[120]. To translate these findings to a 3D model, we developed conductive microfibers as potential sources for electrical signal propagation in hPSC-CM cardiac spheroids. Therefore, we hypothesized that the addition of conductive microfibers to 3D cardiac spheroids could accelerate hPSC-CM maturation while maintaining their high throughput qualities. To achieve this, we created a library of conductive microfibers with various lengths via cryo-sectioning and assessed the effect of microfiber mass and length on cardiac spheroid formation and function. In doing so, we found that cardiac spheroids formed with conductive PEDOT:PSS microfibers exhibited improved contractility parameters over 3D control spheroids without microfibers and cardiac spheroids containing non-conductive PVA microfibers. By further probing the effect of microfibers on spheroid morphology and cardiac protein expression, we observed that conductive PEDOT:PSS cardiac spheroids preferentially formed ring-like structures with a less compacted cavity, aiding in their contractility. Such contractile differences were supported by the increase in contractility and calcium handling protein expression and improved calcium handling, suggesting that conductive polymers may be used to accelerate the maturity of hPSC-CM cardiac spheroids.

3.3 Materials and methods

3.3.1 Preparation of PVA/PEDOT:PSS/PEGDE electrospun scaffolds

Conductive polymer solutions were prepared as previously described[120]. Briefly, PVA (Sigma-Aldrich, 363146) was dissolved in deionized (DI) water and combined with a 3% (w/v) solution of poly(ethylene glycol) diglycidyl ether (PEGDE, Sigma-Aldrich, 475696) in a

PEDOT:PSS 1.3% wt. dispersion in water (Sigma-Aldrich, 483095) to create base 8% (w/v) PVA solutions with 0% or 9.75% mass to mass ratio solutions of PEDOT:PSS to PVA. An Inovenso Nanospinner (KTP700 Basic) electrospinner was utilized for scaffold fabrication at 0.5-0.75mL/hr flow rate, 20cm working distance, 33kV applied voltage, and 30% humidity with a 0.8mm nozzle for a total of 0.5mL solution spun per session. Scaffolds were collected on 18mm coverslips (Fisherbrand, 12545100) and crosslinked in a glass chamber (Chemglass, AF-0556) in the presence of 0.2M glutaraldehyde, subjected to vacuum for 15 seconds, and placed in an oven at 80ºC for 30 minutes. After crosslinking, scaffolds were washed three times for 30 minutes with a 1% (w/v) glycine solution to remove unreacted glutaraldehyde, followed by three 10-minute washes in DI water[76].

3.3.2 Preparation and characterization of conductive microfibers

Crosslinked non-conductive and conductive electrospun scaffolds were frozen in DI water in cryomolds and cryo-sectioned at 5, 10, or 20µm sections with a Leica CM1860 Cryostat to create a library of microfiber lengths. Sections were collected in 15mL conical tubes and the resulting microfiber solutions were filtered with a 100µm strainer. Microfiber solutions were frozen at -80ºC, lyophilized (Labconco) for 5 days and resuspended at 1 mg/mL in sterile DI water. Solutions were vortexed for 1h to disrupt microfiber aggregates. To determine microfiber lengths, brightfield images of 10µL of each solution were measured with ImageJ. Stock solutions were frozen at -80ºC and thawed for future use. For cell culture, microfiber solutions were UV-sterilized for 30 minutes, vortexed for 45min, and diluted in quenching media, described later, containing 1% penicillin-streptomycin (p/s).

3.3.3 hPSC-CM differentiation and conductive spheroid formation

RUES2 hPSCs were expanded on Matrigel-coated 6-well plates (Corning, CLS354234) in mTeSR 1 media (Stemcell Technologies, 85850) with daily changes and maintained as previously described[120]. To produce hPSC-CMs, the GiWi cardiac differentiation protocol was employed[80].

After 15 days of cardiac differentiation, the resulting hPSC-CMs were dissociated to form cardiac spheroids. hPSC-CMs were dissociated in 0.5mL collagenase IV (4 mg/mL, Gibco, 17104-019) for 15min at 37 °C, quenched in RPMI 1640 + B27 supplement +20% fetal bovine serum (FBS) (v/v) + 5μM Y-27632 dihydrochloride, and centrifuged at 400g for 5min. hPSC-CMs were resuspended in the quenching media at 500,000 cells/mL and combined 1:1 with conductive or non-conductive microfiber solutions suspended in quenching media. To determine the effect of microfiber mass on cardiac spheroid maturity, 5μm-sectioned microfiber solution stocks were made at 100, 200, or 400μg/mL; to determine the effect of microfiber length on maturity, microfibers sectioned at 5, 10, or 20μm were resuspended at 200μg/mL. Cardiac spheroids were formed in 96-well round bottom plates (Corning, 7007) by pipetting 200 μL/well of the hPSC-CM+fiber suspension and centrifuged at 200g (Eppendorf, 5810R) for 5min, resulting in cardiac spheroids cell of 50,000 cells/well with 10, 20, or 40μg microfibers/spheroid for varying microfiber mass spheroids and 20μg microfibers/spheroid for varying microfiber length spheroids. Finally, control spheroids lacking microfibers (3D control) were formed. Media was changed to CM maintenance media (RPMI 1640+ B27) after two days of spheroid formation and every other day for 15 days (day 30 of hPSC-CM differentiation) prior to performing assays.

3.3.4 Cardiac spheroid contractility

Brightfield video recordings of cardiac spheroids were captured on days 3, 5, and 15 at 4x on a Nikon Eclipse Ti microscope with a Yokogawa CSU-X1 confocal attachment. The total percentage of beating spheroids per condition was calculated. For cardiac spheroids with varying

microfiber lengths, recordings were analyzed to determine beat frequency (beats per minute, bpm), peak to peak, R90 time to peak, and R50 peak width using a modified code by Ronaldson-Bouchard et. al[121].

3.3.5 Immunofluorescent assays

Day 15 cardiac spheroids were collected, washed with DPBS, and fixed in 4 % paraformaldehyde (Fisher Scientific, O4042-500) in DPBS for 40 min at room temperature. Fixed spheroids were washed with DPBS and stored in 30% sucrose in DPBS overnight at 4°C prior to embedding in optical cutting temperature (OCT, Fisher Scientific, 23-730-571) by freezing on dry ice and isopropyl alcohol for rapid freezing. Embedded spheroids were sectioned at 10μm on a cryostat at -20°C. Sections were collected on charged glass slides (Fisher Scientific, 12-550-15) and stored at -20°C for further processing.

For staining, stored sections were allowed to reach room temperature then washed in cold DPBS for 15min to remove the OCT. A pap pen (Vector Laboratories, H-4000) was used to draw a hydrophobic barrier around the spheroids. Spheroids were permeabilized in 0.25% (v/v) Triton X-100 (Fisher Bioreagents, BP151-100) for 10min and blocked for 1h in DPBS with calcium and magnesium containing 5% (w/v) bovine serum albumin (BSA, Goldbio, A-420-10) and 0.1% (v/v) Triton X-100. Spheroids were incubated in α-actinin (1:400, Sigma-Aldrich, ZRB1169) and myosin heavy chain 7 (MYH7, Santa Cruz Biotechnology, sc-53090) primary antibodies for 2h at room temperature in the blocking buffer. Samples were then incubated in AlexaFluor 488 conjugated donkey anti-mouse (1:500, Invitrogen, A21202) antibody and AlexaFluor 555 conjugated donkey anti-rabbit (1:500, Invitrogen, A-31572) for 2h at room temperature. Samples were finally incubated in Hoechst 33342 in DI water (1:2000, Invitrogen, H3570) for 15min at room temperature, mounted on slides with Fluoromount-G (Southern Biotech, 0100-01), and

allowed to dry overnight prior to immunofluorescent (IF) imaging. An Olympus SLIDEVIEW VS200 and Keyence BZ-X710 microscope were used to perform whole-spheroid imaging at 40x magnification.

3.3.6 Western blotting

Day 15 cardiac spheroids were harvested and lysed for protein identification. Spheroids were transferred to cold eppendorf tubes and spun down at 500g for 3min at 4ºC, washed with cold DPBS, and re-spun at 500g for 3min at 4ºC. DPBS was removed and spheroids were lysed in cold mRIPA buffer by pipetting. Samples were incubated on ice for 20min and vortexed every 5min. Samples were then centrifuged at 21,000g for 15min at 4 ºC to pellet microfibers and cell debris and the supernatant was transferred to a new tube. Protein was combined 1:1 with 4x Laemmli sample buffer (BioRad, 1610747) containing 0.1M dithiothreitol (DTT). Samples were then denatured at 95°C for 10min and 18µl per lane was loaded on a 4–12% Bis-Tris Plus gel (Invitrogen, NW04122BOX). Gels were run at 60V for 2h and transferred using an iBlot nitrocellulose transfer membrane (Invitrogen, IB301001) for 7min. Membranes were blocked using Azure Blot blocking buffer (Azure Biosystems, AC2190) for 1h and incubated with primary antibodies (GAPDH, 1:2000, Abcam, ab8245; MYH7, 1:1000, Santa Cruz, SC-53090; α-actinin, 1:1000, Sigma-Aldrich, ZRB1169; N-cadherin (NCad), 1:1000, Invitrogen, 33-3900, sarcoendoplasmic reticulum calcium ATPase (SERCA2), 1:500, Invitrogen, MA3-919; myosin light chain 2 (MLC2v), 1:1000, Proteintech, 10906-I-AP) overnight at 4°C on an orbital shaker at 50rpm (Southwest Science). Membranes were then incubated in secondary antibodies (1:2000, Invitrogen, A11374 and A10038) for 1h at room temperature on an orbital shaker and imaged using a LI-COR Odyssey. Blots were analyzed using ImageJ and proteins of interest were normalized to GAPDH expression per condition, then normalized to the 3D control spheroid.

Statistical significance was determined using a one-way ANOVA with a Kruskal–Wallis test for three biological replicates.

3.3.7 Calcium handling

Day 15 cardiac spheroids were harvested for calcium handling. Spheroids were transferred to a 96-well glass bottom plate (Cellvis, P96-1.5H-N) and incubated with 4μM fluo-4 AM ester (Biotium, 50018) in CM maintenance media for 15 minutes at 37 ºC in the dark. After 15 minutes, cardiac spheroids were imaged using a Nikon Eclipse Ti microscope with a Yokogawa CSU-X1 confocal attachment at 4x magnification. Ten spheroids per condition across 2 biological replicates were recorded for 30 seconds. In ImageJ, 4 regions of interest (ROIs) per cardiac spheroid were selected and the integrated density values were analyzed using a using a custom MATLAB script.

3.3.8 Statistical analysis

The respective statistical tests and n numbers are described in the figure legends. The following statistical significance cut off was applied: $p > 0.05$, $*p < 0.05$, $**p < 0.01$, $***p < 0.01$, $****p < 0.0001$. Data expressed as box-and-whisker plots show all points with the whisker ends corresponding to minimum and maximum values. All other values are expressed as mean ± SD. Statistical analyses were performed using GraphPad Prism Software v10.0.

3.4 Results and discussion

3.4.1 Cryo-sectioning achieves electrospun scaffold microfiber fragmentation

We previously demonstrated that PEDOT:PSS could be successfully blended with PVA to create conductive, biocompatible electrospun scaffolds for 2D hPSC-CM maturation. Here, we sought to translate these findings into a 3D platform to accelerate the maturation of cardiac spheroids while maintaining a high-throughput cardiac model. To achieve this, we fragmented our existing electrospun scaffolds to create a library of non-conductive and conductive microfibers

that could be incorporated into hPSC-CM cardiac spheroids. While previous methods have been employed to fragment electrospun scaffolds[122], these were not applicable to our crosslinked, non-hydrogel scaffolds. Therefore, we implemented the use of cryo-sectioning to achieve scaffold fragmentation. First, frozen non-conductive 8% PVA and conductive 8% PVA+PEDOT:PSS electrospun scaffolds were sectioned at either 5, 10, or 20µm, strained with a 100µm cell strainer to remove aggregates, and resuspended at a known concentration after lyophilizing over 5 days (Figure 3.1, a). By modulating section size, we created a library of microfibers that were significantly different based on section size, though no differences were observed based on scaffold type (non-conductive vs. conductive) (Figure 3.1, b-c). Further, our 5µm-sectioned conductive microfibers displayed lengths ranging from 2-20µm, similar to those reported for collagen I gels[93,122]. Therefore, we demonstrated that cryo-sectioning is a useful technique to achieve electrospun scaffold fragmentation and changing section size permits for microfibers of various length ranges that can be used to explore the effect of conductive polymers on cardiac spheroid maturation.

3.4.2 Optimization of conductive cardiac spheroids

To determine the optimal microfiber conditions for conductive cardiac spheroids, we investigated the effect of microfiber mass and length on spheroid formation and performance. Day 15 hPSC-CMs were used in the formation of cardiac spheroids to determine the effect of conductive microfibers on hPSC-CM maturation after lineage specification (Figure 3.1, d). With fixed 5µm sectioned microfibers, we assessed cardiac spheroid formation and performance with 10, 20, or 40µg of non-conductive or conductive microfibers per spheroid, and compared them to a 3D control lacking microfibers. By tracking the percentage of beating spheroids over time, we found that spheroids formed with 20 and 40µg of conductive microfibers maintained the highest

percentage of beating constructs over time compared to the 3D control and non-conductive spheroids (Supplemental Figure 3.1, a). However, the largest microfiber mass prevented spheroid compaction and robust spheroid formation; therefore, 20μg of microfibers was chosen to form cardiac spheroids with varying fiber lengths to further probe the effect of microfiber length on cardiac spheroid performance. In this case, all spheroids maintained a similar percentage of beating constructs over time (Supplemental Figure 3.1, b), indicating that 20μg of microfibers is ideal for spheroid formation across variable lengths. Differences in beating percentage in control spheroids lacking microfibers between Supplemental Figure 3.1, a and b are likely a result of batch-to-batch hPSC-CM differentiation variability. In the case of cardiac spheroids with increasing microfiber lengths, we further measured contractility parameters over 15 days to establish the optimized microfiber parameters. Beats per minute increased, while peak to peak, time to peak, and peak width decreased with conductive microfibers (Figure 3.2, a-d); further, while beat frequency and peak to peak were improved with 5μm-sectioned conductive microfibers, time to peak and peak width benefitted most with 10 and 20μm-sectioned conductive microfibers. This suggests an improvement in the contractility of conductive cardiac spheroids compared to control and 8% PVA spheroids. These results were summarized in a heatmap (Figure 3.2, e) by comparing the change in contractility parameter over time between days 3 and 15 post-spheroid formation. By assessing the change in intra-batch parameter variance, we found variance decreased over time in conductive spheroids and was most evident in spheroids formed with 5μm sectioned microfibers (Figure 3.2, f), thus becoming more uniform over time. Since microfibers sectioned at 5μm result in length ranges similar to collagen I gel fibers, this suggests that while recapitulating the morphology of natural extracellular matrix (ECM) fibers is important in both non-conductive and conductive microfiber spheroid formation, functionality is further improved in the presence of PEDOT:PSS,

likely due to its ability to enable electrical cell-cell communication. Overall, by titrating microfiber mass and length, we found that 20μg of microfibers sectioned at 5μm resulted in the optimal cardiac spheroids and were utilized for the remainder assays.

3.4.3 Conductive microfibers lead to structural differences between cardiac spheroids

To determine how microfibers affect cardiac spheroid size, we tracked their compaction differences over time. We found that control cardiac spheroids were smallest after 15 days, while PEDOT:PSS microfiber spheroids remained largest over time (Figure 3.3, a-b). Upon dissociation and cell counting (Supplemental Table 3.1), we found that 3D control and 8% PVA spheroids had higher cell numbers compared to PEDOT:PSS spheroids, suggesting that size differences were not due to proliferation differences between the different conditions. Further, we found that cardiac spheroids formed in the presence of conductive microfibers formed more ring-like structures, with a higher density of cells around the perimeter of the structure compared to the center. We hypothesize that these structural differences are likely due to differences in microfiber stiffness, where conductive PEDOT:PSS microfibers are stiffer than 8% PVA microfibers[120]. With stiffer microfibers, the cells' ability to manipulate and incorporate the microfibers into the center of the construct in diminished, resulting in a denser ring-like construct around a less compacted cavity, evident in their increased diameter compared to 3D control and 8% PVA spheroids. Interestingly, such ring-like structures mimic cavity formation during embryogenesis[118,123] and appear advantageous to the function of our PEDOT:PSS cardiac spheroids. In contrast, by day 15, 3D control spheroids showed weaker contractions, likely due to the increased compaction. IF imaging (Figure 3.4, c) also revealed the presence of non-CM clusters within the 3D control and 8% PVA spheroids, which were less evident in the PEDOT:PSS spheroids, thus illustrating the conductive

microfibers' ability to maintain a higher hPSC-CM population after lineage specification for improved function.

3.4.4 Conductive cardiac spheroids upregulate cardiac-related proteins and aid in calcium handling

Upon optimizing microfiber parameters for cardiac spheroid performance, we sought to determine the effect of conductive microfibers on cardiac protein expression. After 15 days of cardiac spheroid formation, we observed higher cardiac protein expression in conductive cardiac spheroids. Ncad, important in the providing mechanical stability by linking the actin cytoskeleton at intercalated discs and preventing dilated cardiomyopathies[124], was similar across all conditions though remained higher in conductive cardiac spheroids, suggesting a slight improvement in hPSC-CM mechanical coupling for cell-cell communication. Further, it is well established that the presence of calcium handling proteins, such as SERCA2 for proper calcium reuptake back into the sarcoplasmic reticulum[125], are necessary for cell-cell electrical communication and illustrate mature excitation-contraction coupling. Here, we found significant increased SERCA2 protein levels in conductive cardiac spheroids compared to 3D control spheroids, suggesting an improvement in their calcium handling and electrical coupling abilities. In addition to electrical coupling, hPSC-CM maturity and contractility is characterized by the switch of myosin heavy chain 6 (MYH6) to myosin heavy chain 7 (MYH7), as well as the presence of ventricular myosin regulatory light chain 2 (MLC2v)[101]. We found that cardiac spheroids formed with conductive microfibers expressed higher levels of contractile proteins (MYH7, MLC2v, and α-actinin), with MLC2v being statistically significant, compared to 3D control and non-conductive microfiber spheroids (Figure 3.4, a-b). Surprisingly, MYH7 was either not detected or lowly expressed in the 3D control and non-conductive cardiac spheroids compared to conductive cardiac spheroids

(Supplemental Figure 3.2). To support our western blot findings, we performed IF imaging on day 15 cardiac spheroids. IF revealed that all cardiac spheroids express MYH7, suggesting that conductive cardiac spheroids likely maintain a higher percentage of hPSC-CMs, thus resulting in a higher western blot expression (Figure 3.4, c). These findings correlated with our contractility parameter analysis (Figure 3.2) where conductive microfibers resulted in improved contractility and qualitatively stronger contractions; therefore, while the magnitude of α-actinin was similar across all conditions, the higher levels of MYH7 and MLC2v suggest that proper hPSC-CM contractions rely on both the presence of proper crosslinking via α-actinin and functional motor proteins and are aided by the presence of conductive PEDOT:PSS microfibers.

To establish the functional maturity of conductive cardiac spheroids and the role of elevated SERCA2 in conductive cardiac spheroids, we assessed their calcium handling abilities. Kymographs from each condition (Figure 3.5, a) illustrate the low instances of calcium fluxing in 3D control cardiac spheroids. While the number of calcium peaks increased in non-conductive 8% PVA spheroids, these spheroids also experienced asynchronous fluxes throughout the construct (Supplemental Videos 3.1-3.3), while PEDOT:PSS conductive spheroids maintained regular, synchronous fluxes. Of note, the total percentage of fluxing cardiac spheroids measured across two biological replicates was lowest in the 3D control, with no fluxing detected in one biological replicate (Figure 3.5, b). In contrast, the total percentage of fluxing cardiac spheroids was highest in the conductive cardiac spheroid condition. Upon analyzing the flux, we found that cycle length and width significantly decreased in the presence of PEDOT:PSS compared to the control (Figure 3.5, c-d), indicating a higher instance of calcium fluxing and decreased time for calcium reuptake into the sarcoplasmic reticulum. Further, the decrease in peak width time correlated with the increase in SERCA2 expression in PEDOT:PSS cardiac spheroids. Time to peak (Figure 3.5, e)

was similar across all conditions, while dF/F_o, related to intensity of calcium efflux from the sarcoplasmic reticulum, decreased in cardiac spheroids, likely due to the intrinsic dark blue color of PEDOT:PSS that decreased the amount of fluorescent signal detected upon laser excitation. Despite this, these data suggest that conductive polymers support calcium homeostasis by preventing prolonged cytosolic calcium levels that may otherwise lead to the activation of proteases and impaired cardiac function[125], further suggesting improved maturity over control 3D cardiac spheroids without conductive polymers.

3.5 Conclusion

Here, we explored the use of conductive microfibers as a viable source of conductivity to accelerate the functional maturity of hPSC-CM cardiac spheroids. A library of microfibers was achieved through cryo-sectioning electrospun scaffolds to recapitulate the morphology of native ECM fibers while providing a source of conductivity. We found that conductive microfibers were readily incorporated into cardiac spheroids to facilitate cell-cell interactions in distant hPSC-CMs to improve functionality while maintaining a high throughput cardiac spheroid model. The presence of PEDOT:PSS resulted in more ring-like structures with a less compacted inner cavity, which may mimic cavity formation during embryogenesis and facilitating contractility. Likewise, the increased compaction in 3D control and 8% PVA non-conductive cardiac spheroids resulted in decreased contractility. These functional differences were supported through the higher expression of contractile proteins, such as MYH7, MLC2v, and α-actinin, in conductive microfiber cardiac spheroids. Further, an increase in SERCA2 in conductive microfiber cardiac spheroids suggested an improvement in their calcium handling abilities to facilitate cell-cell electrical communication; upon performing calcium handling experiments, the results correlated with the increased SERCA2 protein levels, evidenced through the increased cycle length and decreasing

peak width times, further supporting an improvement in calcium homeostasis. Taken together, these data support that conductive polymer microfibers can accelerate the maturation of cardiac spheroids, compared to control cardiac spheroids without microfibers or with non-conductive microfibers. Additional assays are required to determine how conductive microfibers lead to transcriptional changes over time compared to our control spheroids. Further, given that microfiber stiffness led to differences in cardiac spheroid morphology, it would be of interest to explore whether increasing non-conductive microfiber stiffness also results in these ring-like structures. In doing so, their overall potential as cardiac disease models and as potential therapeutics may be established.

3.6 Figures

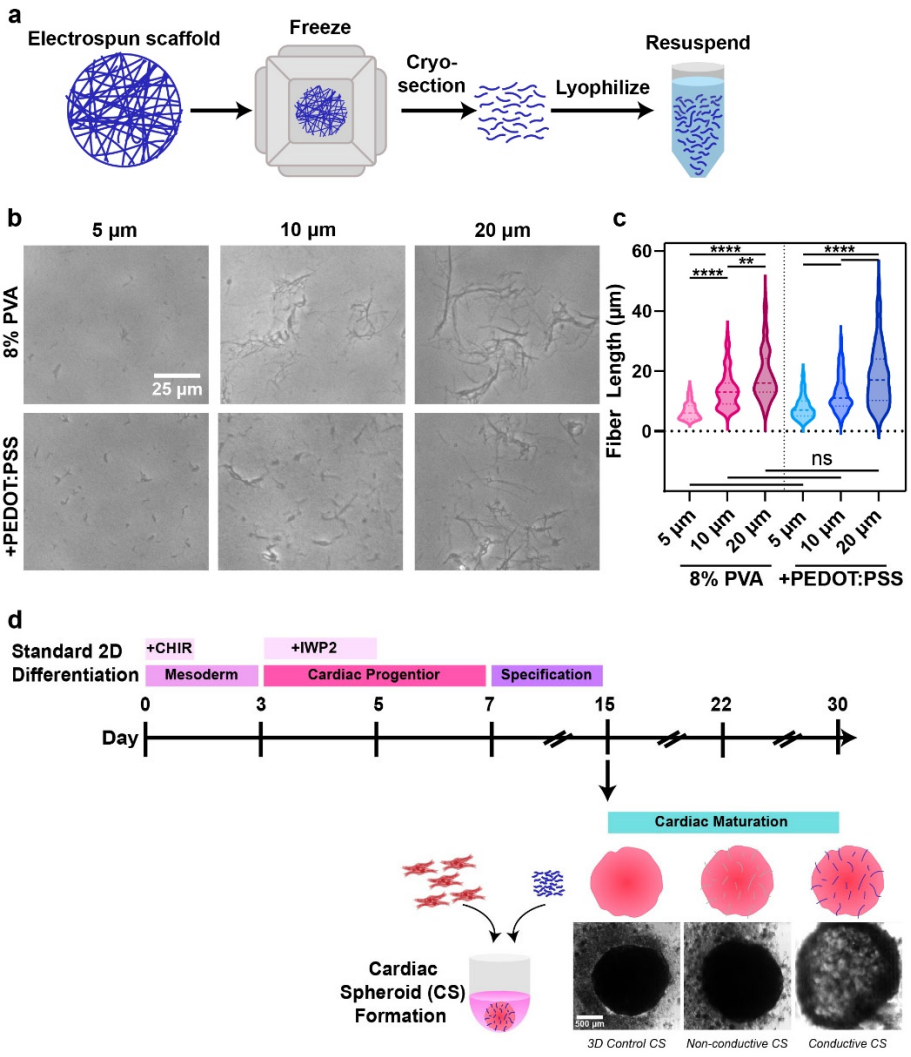


Figure 3.1: Microfiber and cardiac spheroid formation.

(a) Schematic illustrating microfiber formation. Electrospun scaffolds were frozen in DI water in cryomolds and cryo-sectioned at 5, 10, or 20µm section thicknesses. The resulting microfibers solutions were collected, filtered through a 100µm cell strainer, frozen, lyophilized for 5 days, and resuspended at 1 mg/mL in DI water. (b) Brightfield images of non-conductive 8% PVA microfibers or conductive 8% PVA+PEDOT:PSS microfibers after sectioning at 5, 10, or 20µm (scale = 25 µm). (c) Increasing section length increased microfiber length range. 8% PVA microfibers sectioned at 5, 10, and 20µm exhibited median lengths of 6, 13, and 16µm, respectively (n =3, 2, 2 batches). Microfibers containing PEDOT:PSS sectioned at 5, 10, and 20µm exhibited median lengths of 7, 11, and 17 µm (n = 3, 3, 3 batches). Statistical significance was determined via a Kruskal-Wallis with Dunn's multiple comparison test. (d) Cardiac spheroids were formed at day 15 of the standard GiWi hPSC-CM differentiation in the presence of non-conductive, conductive, or no (3D control) microfibers (scale = 500µm).

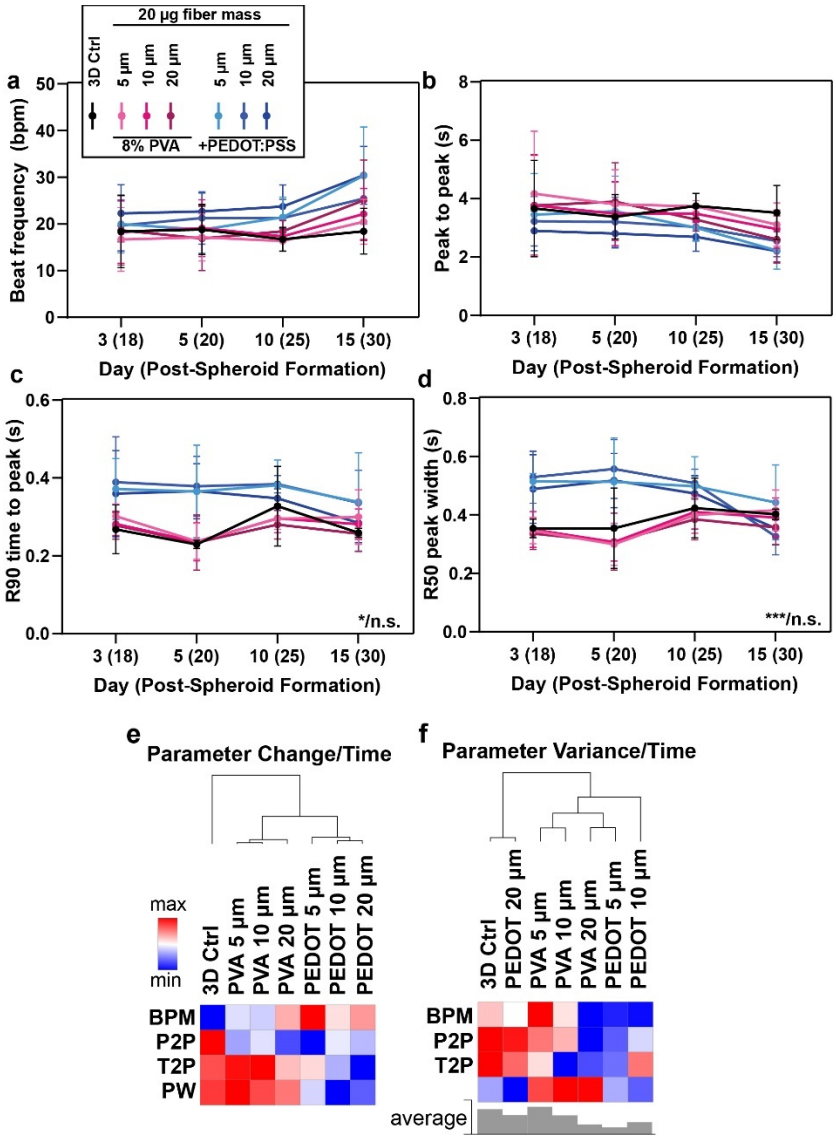


Figure 3.2: Cardiac spheroid contractility parameter change over time.

Cardiac spheroids were formed with 20µg microfibers with 5, 10, or 20µm-sectioned microfibers over 15 days. Beat frequency (beats per minute, BPM, a) was highest in conductive +PEDOT:PSS spheroids and inversely correlated to peak to peak time (b). R90 time to peak (time between 10% of the contraction and peak amplitude, c) and R50 peak width (peak width at half max contraction, d) decreased with increasing conductive microfiber length. Values were calculated across n = 3 biological replicates. Error bars indicate standard deviation from the mean. Statistical significance was determined via a two-way ANOVA with Tukey's multiple comparison test. For (b) and (d), differences were statistically significant due to fiber type compared to time (n.s., not significant). (e) Contractility parameter change over time for cardiac spheroids formed with varying fiber lengths at a fixed 20 µg/spheroid (BPM = beats per minute; P2P = peak to peak; T2P = time to peak; PW = peak width). BPM increases while other parameters decrease with conductive microfibers. (f) Change in parameter variance over time indicates conductive spheroids with 5µm-sectioned microfibers at 20 µg/spheroid experience the largest decrease in variance over time.

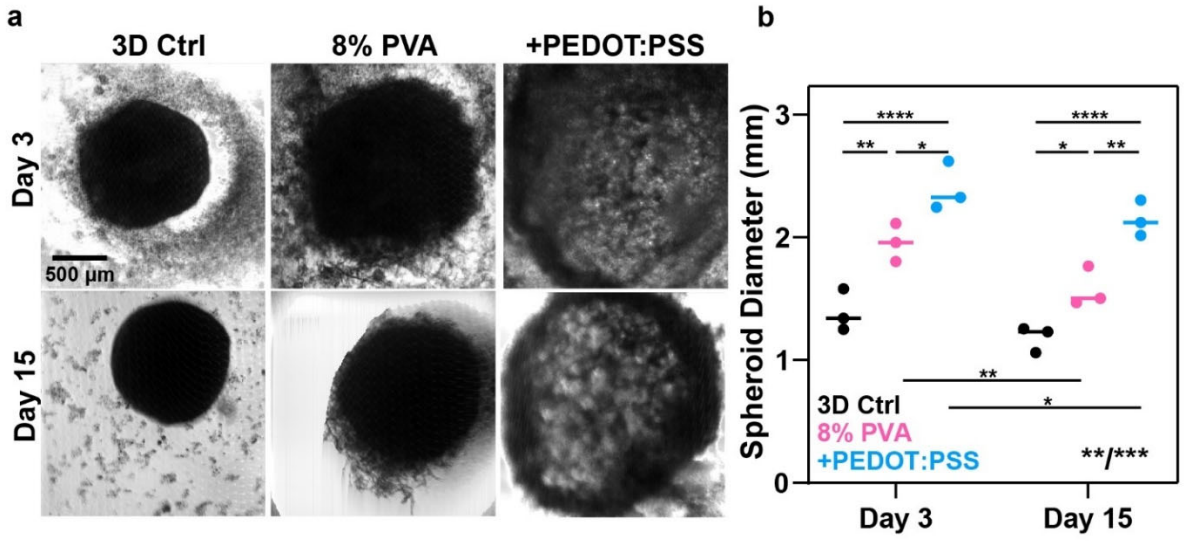


Figure 3.3: Cardiac spheroid compaction over time.

(a) Control, non-conductive, and conductive cardiac spheroids 3 and 15 days after forming with optimized 20 µg, 5-µm sectioned microfibers. (b) Cardiac spheroids compact over 15 days though remain larger in the presence of PEDOT:PSS. Median spheroid diameters for 3D control, 8% PVA, and 8%+PEDOT:PSS were 1340.4, 1959.8, and 2326.7µm at day 3 and 1231, 1504.41, and 2121.9µm by day 15, respectively (n = 3 biological replicates). Statistical significance was determined via a two-way ANOVA with Tukey's multiple comparison test. Time and fiber type comparisons were found to be statistically significant sources of variation.

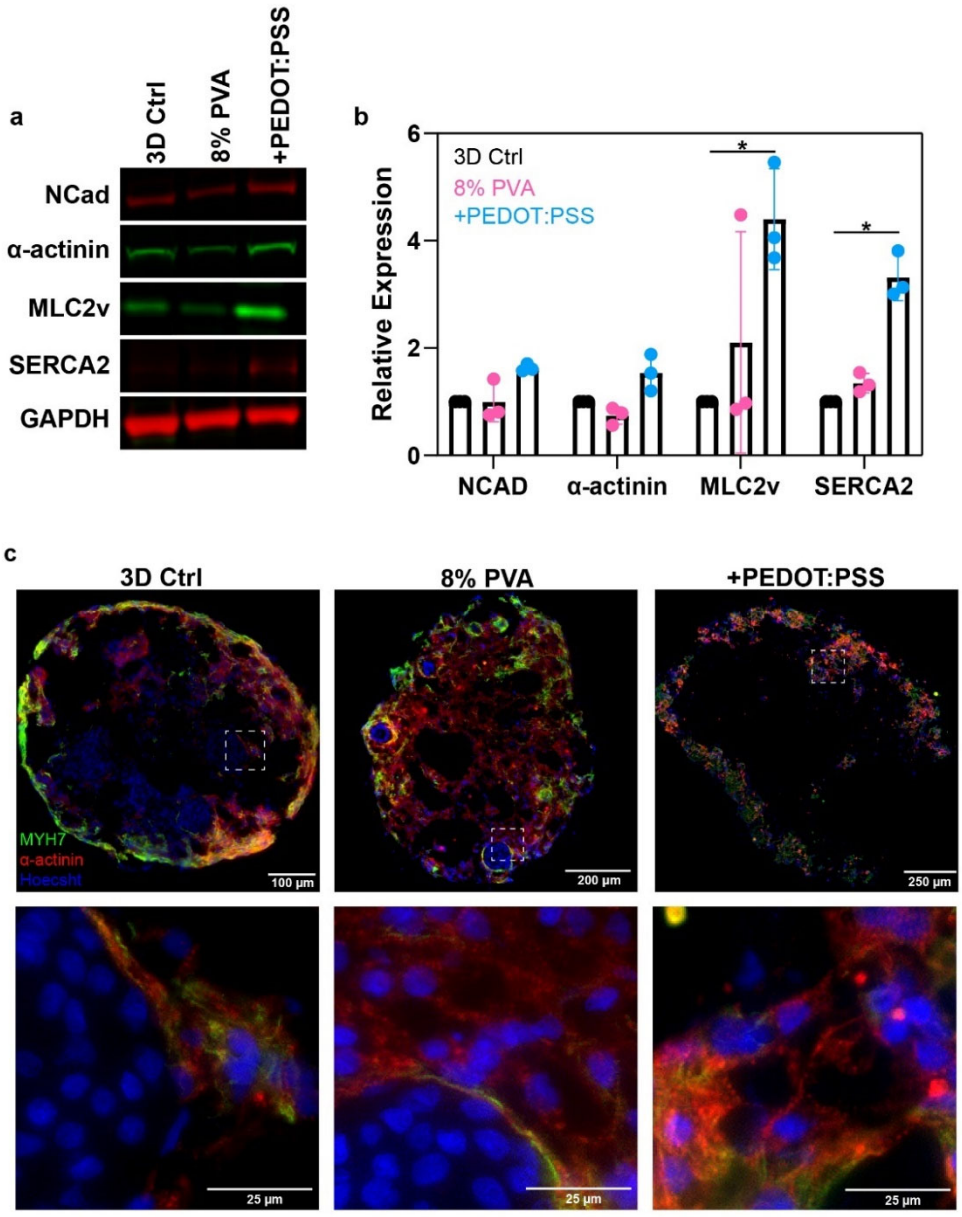


Figure 3.4: Cardiac protein expression increases in conductive cardiac spheroids.

(a) Representative western blot and (b) quantification of N-cadherin (NCad), α-actinin, myosin light chain (MLC2v), and SERCA2 for cardiac spheroids lysed after 15 days of spheroid formation for 3D control, 8% PVA, and 8%+PEDOT:PSS. Values are normalized to 3D control after normalization to GAPDH expression per condition and represented as the mean with standard deviation across three biological replicates. (c) Representative images of cardiac spheroids stained for α-actinin and MYH7 with corresponding scalebars. Bottom row is magnified regions of the above corresponding image. Statistical significance for (b) was determined with a one-way ANOVA with Tukey's multiple comparison test.

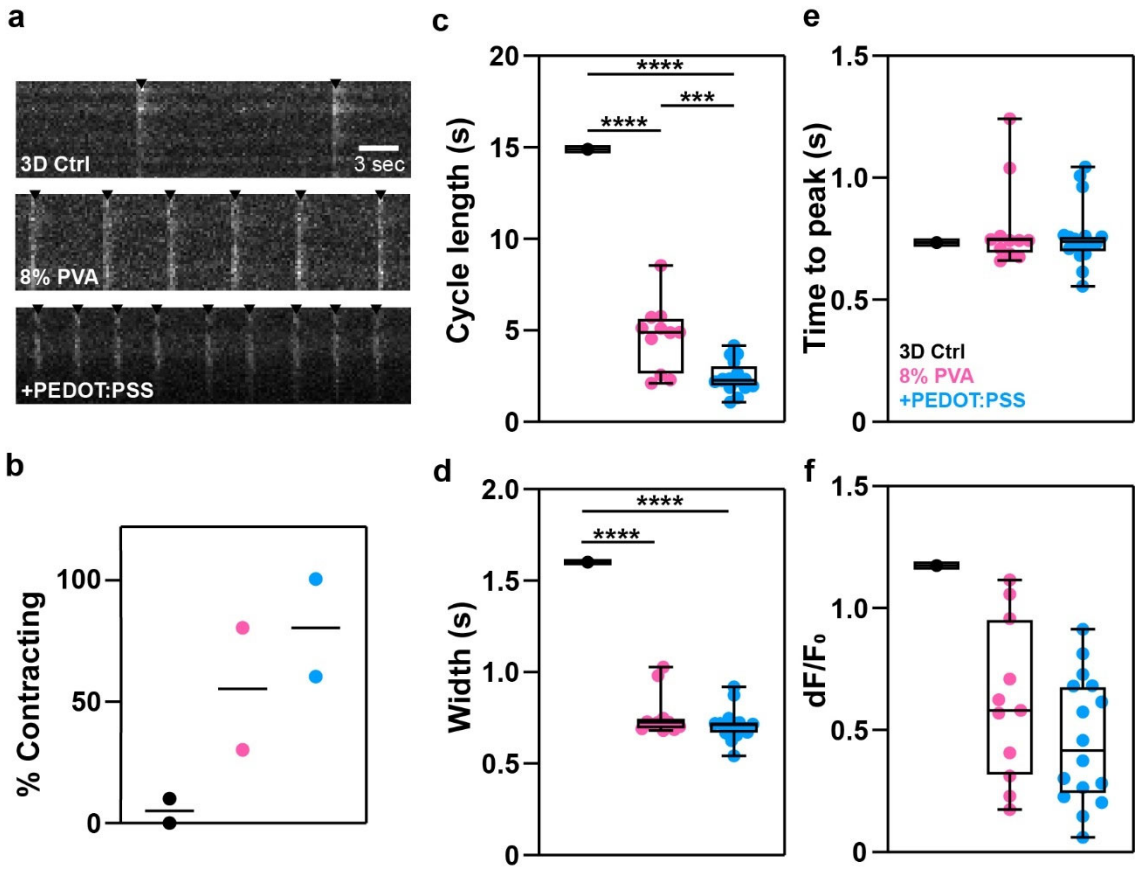


Figure 3.5: Calcium handling performance of cardiac spheroids.

(a) Kymographs of control, 8% PVA, and 8% PVA+PEDOT:PSS cardiac spheroids at 15 days of spheroid formation. Black chevron indicates calcium peak. Scale = 3 seconds. (a) Percentage of contracting spheroids measured across two biological replicates. Ten spheroids per condition and biological replicate were assayed. Cycle length (c) and width (d) decrease in the presence of PEDOT:PSS. Time to peak (e) remained similar across all conditions. dF/F_0 was lowest in conductive cardiac spheroids, likely due to the intrinsic properties of PEDOT:PSS. Each point represents one cardiac spheroid across n = 2 biological replicates. Statistical significance was determined by one-way ANOVA with Tukey's multiple comparison test.

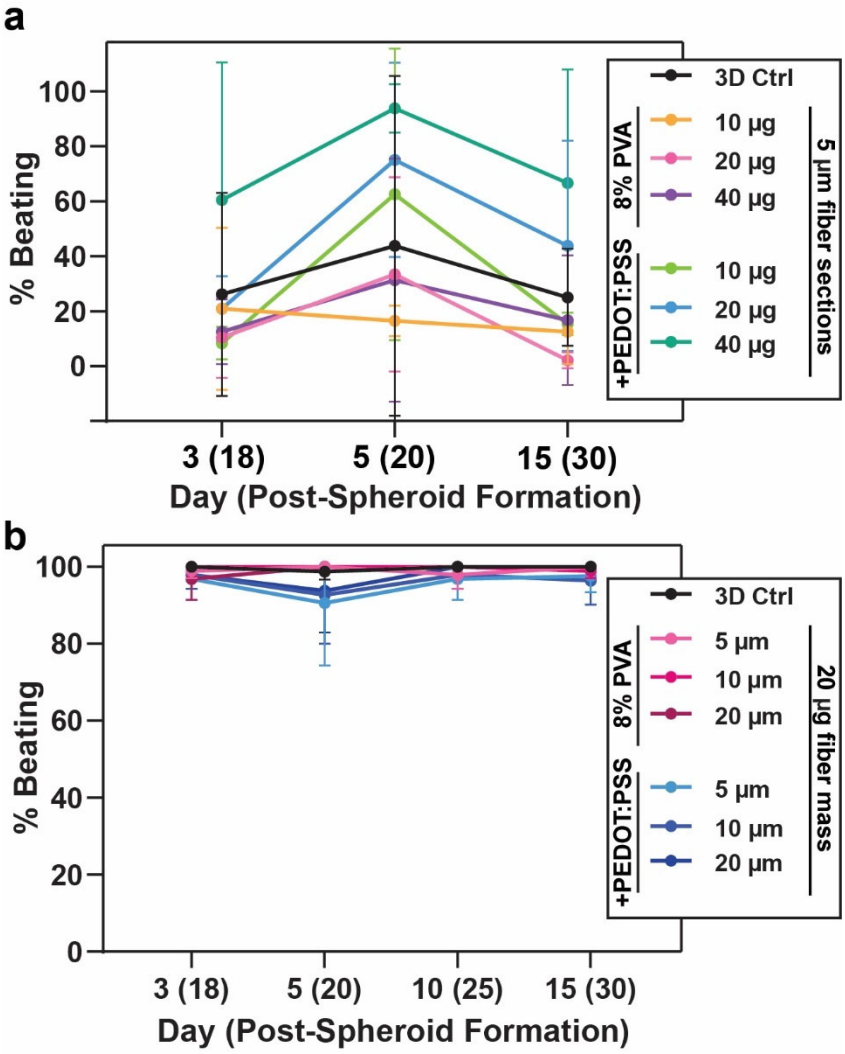
3.7 Tables

Table 3.1: Cell number per cardiac spheroid for each condition across three biological replicates.

Cardiac spheroids were dissociated and their total cell numbers were calculated based on the number of spheroids dissociated per condition. Cell numbers remain lower in conductive PEDOT:PSS cardiac spheroids compared to 3D control and 8% PVA non-conductive spheroids.

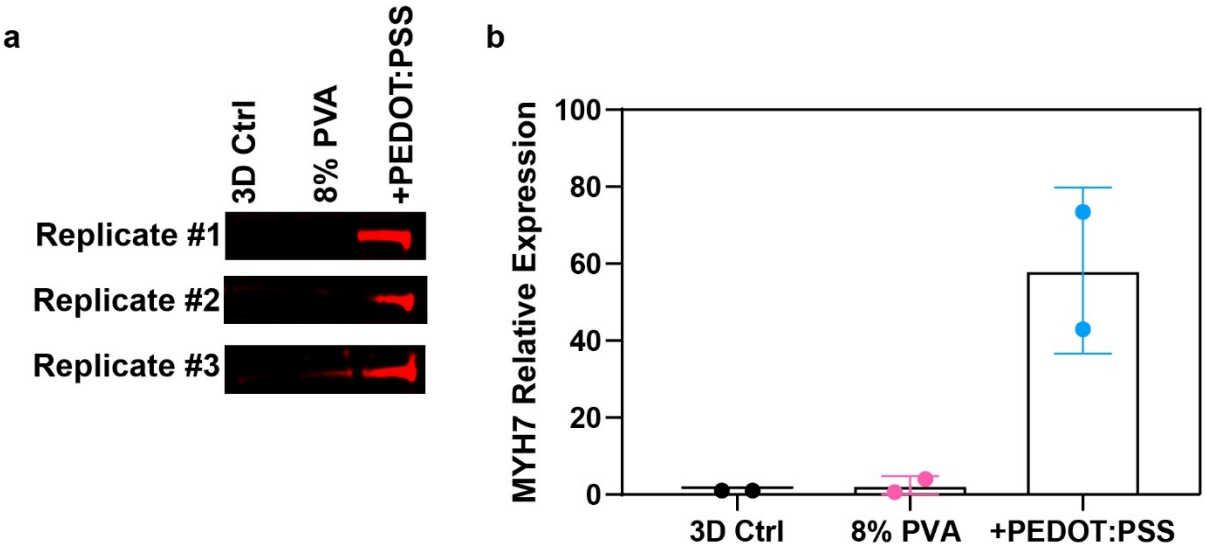
Spheroid Type:	Dissociation #1	Dissociation #2	Dissociation #3
3D Control	10,973	10,750	26,000
8% PVA	7,608	10,266	21,116
+PEDOT:PSS	6,956	3,166	10,928

3.8 Supplemental figures



Supplemental Figure 3.1: Percentage of beating cardiac spheroids with varying fiber mass or length over 15 days.

(a) Percentage of beating non-conductive and conductive cardiac spheroids formed with fixed 5µm-sectioned microfibers at varying microfiber masses over 15 days. The percentage of beating spheroids was highest with 20 and 40µg of conductive microfibers (n = 2 biological replicates). (b) Percentage of beating non-conductive and conductive cardiac spheroids formed with 20µg microfibers at varying lengths over 15 days was similar across all conditions (n=3 biological replicates).



Supplemental Figure 3.2: MYH7 expression for cardiac spheroids.

(a) Representative western blot bands for MYH7 across three biological replicates for 3D control, 8% PVA, and 8% PVA+PEDOT:PSS cardiac spheroids. Relative expression was determined for 2/3 replicates (no detectable signal for 3D control and 8% PVA cardiac spheroids in replicate #1) by normalizing to GAPDH expression per condition and plotted relative to the 3D control. In all cases, MYH7 expression remained higher in PEDOT:PSS cardiac spheroids. Brightness in images was increased by equal amounts in all replicates to illustrate low signal in 3D control and 8% PVA condition.

3.9 Acknowledgements

Chapter 3, in full, is currently being prepared for publication. Gonzalez G, Holman AR, LaMontagne E, Molley TG, Engler AJ. Conductive microfibers improve stem cell-derived cardiac spheroid maturation. The dissertation author was the primary researcher and author of this paper.

The authors would like to thank Dr. Neil Chi (UCSD) for the donation of the RUES2 ESCs, Dr. Karen Christman (UCSD) for access to the Olympus microscope and Labconco lyophilizer, Dr. Max Rempel (Sanford Consortium Stem Cell Core) for access and maintenance of the Keyence microscope, and Dr. Brian Aguado for access to the Leica CM1860 Cryostat. The authors acknowledge funding and equipment support from the National Institutes of Health (R01AG045428 to A.J.E.). Fellowship support was provided by the National Science Foundation (to G.G. and E.L.), the San Diego Fellowship (to G.G.), and the National Institutes of Health (F31 HL163996 to A.R.H.).

REFERENCES

(1) Chong, J. J. H. H.; Yang, X.; Don, C. W.; Minami, E.; Liu, Y.-W. W.; Weyers, J. J.; Mahoney, W. M.; Van Biber, B.; Cook, S. M.; Palpant, N. J.; Gantz, J. A.; Fugate, J. A.; Muskheli, V.; Gough, G. M.; Vogel, K. W.; Astley, C. A.; Hotchkiss, C. E.; Baldessari, A.; Pabon, L.; Reinecke, H.; Gill, E. A.; Nelson, V.; Kiem, H.-P. P.; Laflamme, M. A.; Murry, C. E. Human Embryonic-Stem-Cell-Derived Cardiomyocytes Regenerate Non-Human Primate Hearts. *Nature* **2014**, *510* (7504), 273–277. https://doi.org/10.1038/nature13233.

(2) Liu, Y. W.; Chen, B.; Yang, X.; Fugate, J. A.; Kalucki, F. A.; Futakuchi-Tsuchida, A.; Couture, L.; Vogel, K. W.; Astley, C. A.; Baldessari, A.; Ogle, J.; Don, C. W.; Steinberg, Z. L.; Seslar, S. P.; Tuck, S. A.; Tsuchida, H.; Naumova, A. V.; Dupras, S. K.; Lyu, M. S.; Lee, J.; Hailey, D. W.; Reinecke, H.; Pabon, L.; Fryer, B. H.; MacLellan, W. R.; Thies, R. S.; Murry, C. E. Human Embryonic Stem Cell-Derived Cardiomyocytes Restore Function in Infarcted Hearts of Non-Human Primates. *Nature Biotechnology* **2018**, *36* (7), 597–605. https://doi.org/10.1038/nbt.4162.

(3) Tiscornia, G.; Vivas, E. L.; Belmonte, J. C. I. Diseases in a Dish: Modeling Human Genetic Disorders Using Induced Pluripotent Cells. *Nature Medicine* **2011**, *17* (12), 1570–1576. https://doi.org/10.1038/nm.2504.

(4) Burridge, P. W.; Matsa, E.; Shukla, P.; Lin, Z. C.; Churko, J. M.; Ebert, A. D.; Lan, F.; Diecke, S.; Huber, B.; Mordwinkin, N. M.; Plews, J. R.; Abilez, O. J.; Cui, B.; Gold, J. D.; Wu, J. C. Chemically Defined Generation of Human Cardiomyocytes. *Nature Methods* **2014**, *11* (8), 855–860. https://doi.org/10.1038/nMeth.2999.

(5) Guo, Y.; Pu, W. T. Cardiomyocyte Maturation New Phase in Development. *Circulation Research* **2020**, *126* (8), 1086–1106. https://doi.org/10.1161/CIRCRESAHA.119.315862.

(6) Lian, X.; Hsiao, C.; Wilson, G.; Zhu, K.; Hazeltine, L. B.; Azarin, S. M.; Raval, K. K.; Zhang, J.; Kamp, T. J.; Palecek, S. P. Robust Cardiomyocyte Differentiation from Human Pluripotent Stem Cells via Temporal Modulation of Canonical Wnt Signaling. *Proceedings of the National Academy of Sciences of the United States of America* **2012**, *109* (27), E1848-57. https://doi.org/10.1073/pnas.1200250109.

(7) Shiba, Y.; Gomibuchi, T.; Seto, T.; Wada, Y.; Ichimura, H.; Tanaka, Y.; Ogasawara, T.; Okada, K.; Shiba, N.; Sakamoto, K.; Ido, D.; Shiina, T.; Ohkura, M.; Nakai, J.; Uno, N.; Kazuki, Y.; Oshimura, M.; Minami, I.; Ikeda, U. Allogeneic Transplantation of iPS Cell-Derived Cardiomyocytes Regenerates Primate Hearts. *Nature* **2016**, *538* (7625), 388–391. https://doi.org/10.1038/nature19815.

(8) Shiba, Y.; Fernandes, S.; Zhu, W. Z.; Filice, D.; Muskheli, V.; Kim, J.; Palpant, N. J.; Gantz, J.; Moyes, K. W.; Reinecke, H.; Van Biber, B.; Dardas, T.; Mignone, J. L.; Izawa, A.; Hanna, R.; Viswanathan, M.; Gold, J. D.; Kotlikoff, M. I.; Sarvazyan, N.; Kay, M. W.; Murry, C. E.; Laflamme, M. A. Human ES-Cell-Derived Cardiomyocytes Electrically Couple and Suppress Arrhythmias in Injured Hearts. *Nature* **2012**, *489* (7415), 322–325. https://doi.org/10.1038/nature11317.

(9) Caspi, O.; Huber, I.; Kehat, I.; Habib, M.; Arbel, G.; Gepstein, A.; Yankelson, L.; Aronson, D.; Beyar, R.; Gepstein, L. Transplantation of Human Embryonic Stem Cell-Derived Cardiomyocytes Improves Myocardial Performance in Infarcted Rat Hearts. *Journal of the American College of Cardiology* **2007**, *50* (19), 1884–1893. https://doi.org/10.1016/j.jacc.2007.07.054.

(10) Kehat, I.; Kenyagin-Karsenti, D.; Snir, M.; Segev, H.; Amit, M.; Gepstein, A.; Livne, E.; Binah, O.; Itskovitz-Eldor, J.; Gepstein, L. Human Embryonic Stem Cells Can Differentiate into Myocytes with Structural and Functional Properties of Cardiomyocytes. *Journal of Clinical Investigation* **2001**, *108* (3), 407–414. https://doi.org/10.1172/JCI200112131.
(11) Rajala, K.; Pekkanen-Mattila, M.; Aalto-Setälä, K. Cardiac Differentiation of Pluripotent Stem Cells. *Stem Cells International* **2011**, *2011* (1). https://doi.org/10.4061/2011/383709.
(12) Kadari, A.; Mekala, S.; Wagner, N.; Malan, D.; Köth, J.; Doll, K.; Stappert, L.; Eckert, D.; Peitz, M.; Matthes, J.; Sasse, P.; Herzig, S.; Brüstle, O.; Ergün, S.; Edenhofer, F. Robust Generation of Cardiomyocytes from Human iPS Cells Requires Precise Modulation of BMP and WNT Signaling. *Stem Cell Reviews and Reports 2014 11:4* **2014**, *11* (4), 560–569. https://doi.org/10.1007/S12015-014-9564-6.
(13) Loh, K. M.; Chen, A.; Koh, P. W.; Deng, T. Z.; Sinha, R.; Tsai, J. M.; Barkal, A. A.; Shen, K. Y.; Jain, R.; Morganti, R. M.; Ng, S.-C.; Fernhoff, N. B.; George, B. M.; Wernig, G.; Salomon, R. E.; Chen, Z.; Vogel, H.; Epstein, J. A.; Kundaje, A.; Talbot, W. S.; Beachy, P. A.; Ang, L. T.; Weissman, I. L. Mapping Routes from Pluripotency to Human Bone, Heart and Other Mesoderm Cell Types. *Cell* **2016**, *166* (2), 451–467. https://doi.org/10.1016/j.cell.2016.06.011.Mapping.
(14) Mummery, C.; Ward-van Oostwaard, D.; Doevendans, P.; Spijker, R.; Van den Brink, S.; Hassink, R.; Van der Heyden, M.; Opthof, T.; Pera, M.; Brutel de la Riviere, A.; Passier, R.; Tertoolen, L. Differentiation of Human Embryonic Stem Cells to Cardiomyocytes: Role of Coculture with Visceral Endoderm-like Cells. *Circulation* **2003**, *107* (21), 2733–2740. https://doi.org/10.1161/01.cir.0000068356.38592.68.
(15) Laflamme, M. A.; Chen, K. Y.; Naumova, A. V; Muskheli, V.; Fugate, J. A.; Dupras, S. K.; Reinecke, H.; Xu, C.; Hassanipour, M.; Police, S.; O'Sullivan, C.; Collins, L.; Chen, Y.; Minami, E.; Gill, E. A.; Ueno, S.; Yuan, C.; Gold, J.; Murry, C. E. Cardiomyocytes Derived from Human Embryonic Stem Cells in Pro-Survival Factors Enhance Function of Infarcted Rat Hearts. *Nature Biotechnology* **2007**, *25* (9), 1015–1024. https://doi.org/10.1038/nbt1327.
(16) Karbassi, E.; Fenix, A.; Marchiano, S.; Muraoka, N.; Nakamura, K.; Yang, X.; Murry, C. E. *Cardiomyocyte Maturation: Advances in Knowledge and Implications for Regenerative Medicine*; Nature Research, 2020; Vol. 17, pp 341–359. https://doi.org/10.1038/s41569-019-0331-x.
(17) Yang, X.; Pabon, L.; Murry, C. E. Engineering Adolescence: Maturation of Human Pluripotent Stem Cell–Derived Cardiomyocytes. *Circulation Research* **2014**, *114* (3), 511–523. https://doi.org/10.1161/CIRCRESAHA.114.300558.
(18) Sacchetto, C.; Vitiello, L.; de Windt, L. J.; Rampazzo, A.; Calore, M. Modeling Cardiovascular Diseases with hiPSC-Derived Cardiomyocytes in 2D and 3D Cultures. *International journal of molecular sciences* **2020**, *21* (9). https://doi.org/10.3390/IJMS21093404.
(19) Kattman, S. J.; Witty, A. D.; Gagliardi, M.; Dubois, N. C.; Niapour, M.; Hotta, A.; Ellis, J.; Keller, G. Stage-Specific Optimization of Activin/Nodal and BMP Signaling Promotes Cardiac Differentiation of Mouse and Human Pluripotent Stem Cell Lines. *Cell Stem Cell* **2011**, *8* (2), 228–240. https://doi.org/10.1016/j.stem.2010.12.008.
(20) Lee, J. H.; Protze, S. I.; Laksman, Z.; Backx, P. H.; Keller, G. M. Human Pluripotent Stem Cell-Derived Atrial and Ventricular Cardiomyocytes Develop from Distinct Mesoderm

Populations. *Cell Stem Cell* **2017**, *21* (2), 179-194.e4. https://doi.org/10.1016/j.stem.2017.07.003.
(21) Hofbauer, P.; Jahnel, S. M.; Papai, N.; Salic, S.; Novatchkova, M.; Correspondence, S. M. Cardioids Reveal Self-Organizing Principles of Human Cardiogenesis. *Cell* **2021**, *184*, 1–19. https://doi.org/10.1016/j.cell.2021.04.034.
(22) Drakhlis, L.; Biswanath, S.; Farr, C.-M.; Lupanow, V.; Teske, J.; Ritzenhoff, K.; Franke, A.; Manstein, F.; Bolesani, E.; Kempf, H.; Liebscher, S.; Schenke-Layland, K.; Hegermann, J.; Nolte, L.; Meyer, H.; Roche, J.; Thiemann, S.; Wahl-Schott, C.; Martin, U.; Zweigerdt, R. Human Heart-Forming Organoids Recapitulate Early Heart and Foregut Development. *Nature Biotechnology* **2021**, *39*, 737–746. https://doi.org/10.1038/s41587-021-00815-9.
(23) Fong, A. H.; Romero-López, M.; Heylman, C. M.; Keating, M.; Tran, D.; Sobrino, A.; Tran, A. Q.; Pham, H. H.; Fimbres, C.; Gershon, P. D.; Botvinick, E. L.; George, S. C.; Hughes, C. C. W. Three-Dimensional Adult Cardiac Extracellular Matrix Promotes Maturation of Human Induced Pluripotent Stem Cell-Derived Cardiomyocytes. *Tissue Engineering - Part A* **2016**, *22* (15–16), 1016–1025. https://doi.org/10.1089/ten.tea.2016.0027.
(24) Ronaldson-Bouchard, K.; Ma, S. P.; Yeager, K.; Chen, T.; Song, L. J.; Sirabella, D.; Morikawa, K.; Teles, D.; Yazawa, M.; Vunjak-Novakovic, G. Advanced Maturation of Human Cardiac Tissue Grown from Pluripotent Stem Cells. *Nature* **2018**, *556* (7700), 239–243. https://doi.org/10.1038/s41586-018-0016-3.
(25) Huang, C. Y.; Peres Moreno Maia-Joca, R.; Ong, C. S.; Wilson, I.; DiSilvestre, D.; Tomaselli, G. F.; Reich, D. H. Enhancement of Human iPSC-Derived Cardiomyocyte Maturation by Chemical Conditioning in a 3D Environment. *Journal of Molecular and Cellular Cardiology* **2019**, *138*, 1–11. https://doi.org/10.1016/j.yjmcc.2019.10.001.
(26) Mikryukov, A. A.; Mazine, A.; Wei, B.; Yang, D.; Miao, Y.; Gu, M.; Keller, G. M. BMP10 Signaling Promotes the Development of Endocardial Cells from Human Pluripotent Stem Cell-Derived Cardiovascular Progenitors. *Stem Cell* **2021**, *28*, 96-111.e7. https://doi.org/10.1016/j.stem.2020.10.003.
(27) Sullivan, K. E.; Black, L. D. The Role of Cardiac Fibroblasts in Extracellular Matrix-Mediated Signaling during Normal and Pathological Cardiac Development. *Journal of Biomechanical Engineering* **2013**, *135* (7). https://doi.org/10.1115/1.4024349.
(28) Radisic, M.; Park, H.; Martens, T. P.; Salazar-Lazaro, J. E.; Geng, W.; Wang, Y.; Langer, R.; Freed, L. E.; Vunjak-Novakovic, G. Pre-Treatment of Synthetic Elastomeric Scaffolds by Cardiac Fibroblasts Improves Engineered Heart Tissue. *Journal of Biomedical Materials Research - Part A* **2008**, *86* (3), 713–724. https://doi.org/10.1002/jbm.a.31578.
(29) Talman, V.; Kivelä, R. Cardiomyocyte—Endothelial Cell Interactions in Cardiac Remodeling and Regeneration. *Frontiers in Cardiovascular Medicine*. Frontiers Media S.A. July 26, 2018, p 101. https://doi.org/10.3389/fcvm.2018.00101.
(30) Abecasis, B.; Gomes-Alves, P.; Rosa, S.; Gouveia, P. J.; Ferreira, L.; Serra, M.; Alves, P. M. Unveiling the Molecular Crosstalk in a Human Induced Pluripotent Stem Cell-derived Cardiac Model. *Biotechnology and Bioengineering* **2019**, *116* (5), 1245–1252. https://doi.org/10.1002/bit.26929.
(31) Iyer, R. K.; Odedra, D.; Chiu, L. L. Y.; Vunjak-Novakovic, G.; Radisic, M. Vascular Endothelial Growth Factor Secretion by Nonmyocytes Modulates Connexin-43 Levels in

Cardiac Organoids. *Tissue Engineering Part A* **2012**, *18* (17–18), 1771–1783. https://doi.org/10.1089/ten.tea.2011.0468.
(32) Young, J. L.; Engler, A. J. Hydrogels with Time-Dependent Material Properties Enhance Cardiomyocyte Differentiation in Vitro. **2010**. https://doi.org/10.1016/j.biomaterials.2010.10.020.
(33) Shapira-Schweitzer, K.; Seliktar, D. Matrix Stiffness Affects Spontaneous Contraction of Cardiomyocytes Cultured within a PEGylated Fibrinogen Biomaterial. *Acta Biomaterialia* **2007**, *3* (1), 33–41. https://doi.org/10.1016/j.actbio.2006.09.003.
(34) Rodriguez, M. L.; Beussman, K. M.; Chun, K. S.; Walzer, M. S.; Yang, X.; Murry, C. E.; Sniadecki, N. J. Substrate Stiffness, Cell Anisotropy, and Cell-Cell Contact Contribute to Enhanced Structural and Calcium Handling Properties of Human Embryonic Stem Cell-Derived Cardiomyocytes. *ACS Biomaterials Science and Engineering* **2019**, *5* (8), 3876–3888. https://doi.org/10.1021/ACSBIOMATERIALS.8B01256/SUPPL_FILE/AB8B01256_SI_001.PDF.
(35) Ribeiro, A. J. S.; Ang, Y. S.; Fu, J. D.; Rivas, R. N.; Mohamed, T. M. A.; Higgs, G. C.; Srivastava, D.; Pruitt, B. L. Contractility of Single Cardiomyocytes Differentiated from Pluripotent Stem Cells Depends on Physiological Shape and Substrate Stiffness. *Proceedings of the National Academy of Sciences of the United States of America* **2015**, *112* (41), 12705–12710. https://doi.org/10.1073/pnas.1508073112.
(36) Thavandiran, N.; Dubois, N.; Mikryukov, A.; Massé, S.; Beca, B.; Simmons, C. A.; Deshpande, V. S.; McGarry, J. P.; Chen, C. S.; Nanthakumar, K.; Keller, G. M.; Radisic, M.; Zandstra, P. W. Design and Formulation of Functional Pluripotent Stem Cell-Derived Cardiac Microtissues. *Proceedings of the National Academy of Sciences of the United States of America* **2013**, *110* (49). https://doi.org/10.1073/PNAS.1311120110.
(37) Goldfracht, I.; Protze, S.; Shiti, A.; Setter, N.; Gruber, A.; Shaheen, N.; Nartiss, Y.; Keller, G.; Gepstein, L. Generating Ring-Shaped Engineered Heart Tissues from Ventricular and Atrial Human Pluripotent Stem Cell-Derived Cardiomyocytes. *Nature Communications* **2020**, *11* (1), 1–15. https://doi.org/10.1038/s41467-019-13868-x.
(38) Hansen, A.; Eder, A.; Bönstrup, M.; Flato, M.; Mewe, M.; Schaaf, S.; Aksehirlioglu, B.; Schwörer, A.; Uebeler, J.; Eschenhagen, T. Development of a Drug Screening Platform Based on Engineered Heart Tissue. *Circulation Research* **2010**, *107* (1), 35–44. https://doi.org/10.1161/CIRCRESAHA.109.211458.
(39) Obenaus, A. M.; Mollica, M. Y.; Sniadecki, N. J. (De)Form and Function: Measuring Cellular Forces with Deformable Materials and Deformable Structures. *Advanced Healthcare Materials* **2020**.
(40) Leonard, A.; Bertero, A.; Powers, J. D.; Beussman, K. M.; Bhandari, S.; Regnier, M.; Murry, C. E.; Sniadecki, N. J. Afterload Promotes Maturation of Human Induced Pluripotent Stem Cell Derived Cardiomyocytes in Engineered Heart Tissues. *Journal of Molecular and Cellular Cardiology* **2018**, *118* (November 2017), 147–158. https://doi.org/10.1016/j.yjmcc.2018.03.016.
(41) Carlos-Oliveira, M.; Lozano-Juan, F.; Occhetta, P.; Visone, R.; Rasponi, M. Current Strategies of Mechanical Stimulation for Maturation of Cardiac Microtissues. *Biophysical Reviews* **2021**, *13* (5), 717–727. https://doi.org/10.1007/S12551-021-00841-6/FIGURES/4.

(42) Tsui, J. H.; Leonard, A.; Camp, N. D.; Long, J. T.; Nawas, Z. Y.; Chavanachat, R.; Smith, A. S. T.; Choi, J. S.; Dong, Z.; Ahn, E. H.; Wolf-Yadlin, A.; Murry, C. E.; Sniadecki, N. J.; Kim, D. H. Tunable Electroconductive Decellularized Extracellular Matrix Hydrogels for Engineering Human Cardiac Microphysiological Systems. *Biomaterials* **2021**, *272* (August 2020). https://doi.org/10.1016/j.biomaterials.2021.120764.

(43) Roshanbinfar, K.; Vogt, L.; Greber, B.; Diecke, S.; Boccaccini, A. R.; Scheibel, T.; Engel, F. B. Electroconductive Biohybrid Hydrogel for Enhanced Maturation and Beating Properties of Engineered Cardiac Tissues. *Advanced Functional Materials* **2018**, *28* (42). https://doi.org/10.1002/ADFM.201803951.

(44) Wang, L.; Wu, Y.; Hu, T.; Guo, B.; Ma, P. X. Electrospun Conductive Nanofibrous Scaffolds for Engineering Cardiac Tissue and 3D Bioactuators. *Acta Biomaterialia* **2017**, *59*, 68–81. https://doi.org/10.1016/j.actbio.2017.06.036.

(45) Mawad, D.; Mansfield, C.; Lauto, A.; Perbellini, F.; Nelson, G. W.; Tonkin, J.; Bello, S. O.; Carrad, D. J.; Micolich, A. P.; Mahat, M. M.; Furman, J.; Payne, D. J.; Lyon, A. R.; Gooding, J. J.; Harding, S. E.; Terracciano, C. M.; Stevens, M. M. A Conducting Polymer with Enhanced Electronic Stability Applied in Cardiac Models. *Science Advances* **2016**, *2* (11). https://doi.org/10.1126/sciadv.1601007.

(46) Ruan, J. L.; Tulloch, N. L.; Razumova, M. V.; Saiget, M.; Muskheli, V.; Pabon, L.; Reinecke, H.; Regnier, M.; Murry, C. E. Mechanical Stress Conditioning and Electrical Stimulation Promote Contractility and Force Maturation of Induced Pluripotent Stem Cell-Derived Human Cardiac Tissue. *Circulation* **2016**, *134* (20), 1557–1567. https://doi.org/10.1161/CIRCULATIONAHA.114.014998.

(47) Nunes, S. S.; Miklas, J. W.; Liu, J.; Aschar-Sobbi, R.; Xiao, Y.; Zhang, B.; Jiang, J.; Massé, S.; Gagliardi, M.; Hsieh, A.; Thavandiran, N.; Laflamme, M. A.; Nanthakumar, K.; Gross, G. J.; Backx, P. H.; Keller, G.; Radisic, M. Biowire: A Platform for Maturation of Human Pluripotent Stem Cell-Derived Cardiomyocytes. *Nature Methods* **2013**, *10* (8), 781–787. https://doi.org/10.1038/nmeth.2524.

(48) Radisic, M.; Park, H.; Shing, H.; Consi, T.; Schoen, F. J.; Langer, R.; Freed, L. E.; Vunjak-Novakovic, G. Functional Assembly of Engineered Myocardium by Electrical Stimulation of Cardiac Myocytes Cultured on Scaffolds. *Proceedings of the National Academy of Sciences of the United States of America* **2004**, *101* (52), 18129–18134. https://doi.org/10.1073/PNAS.0407817101/SUPPL_FILE/07817FIG7.JPG.

(49) Llucià-Valldeperas, A.; Soler-Botija, C.; Gálvez-Montón, C.; Roura, S.; Prat-Vidal, C.; Perea-Gil, I.; Sanchez, B.; Bragos, R.; Vunjak-Novakovic, G.; Bayes-Genis, A. Electromechanical Conditioning of Adult Progenitor Cells Improves Recovery of Cardiac Function After Myocardial Infarction. *Stem Cells Transl Med* **2017**, *6*, 970–981.

(50) Cortes, D.; McTiernan, C. D.; Ruel, M.; Franco, W.; Chu, C.; Liang, W.; Suuronen, E. J.; Alarcon, E. I. BEaTS-α an Open Access 3D Printed Device for in Vitro Electromechanical Stimulation of Human Induced Pluripotent Stem Cells. *Scientific Reports* **2020**, *10* (1), 1–8. https://doi.org/10.1038/s41598-020-67169-1.

(51) Skylar-Scott, M. A.; Uzel, S. G. M.; Nam, L. L.; Ahrens, J. H.; Truby, R. L.; Damaraju, S.; Lewis, J. A. Biomanufacturing of Organ-Specific Tissues with High Cellular Density and Embedded Vascular Channels. *Science Advances* **2019**, *5* (9). https://doi.org/10.1126/sciadv.aaw2459.

(52) Miller, J. S. The Billion Cell Construct: Will Three-Dimensional Printing Get Us There? *PLoS Biology* **2014**, *12* (6), 1–9. https://doi.org/10.1371/journal.pbio.1001882.

(53) Yanamandala, M.; Zhu, W.; Garry, D. J.; Kamp, T. J.; Hare, J. M.; Jun, H. wook; Yoon, Y. sup; Bursac, N.; Prabhu, S. D.; Dorn, G. W.; Bolli, R.; Kitsis, R. N.; Zhang, J. Overcoming the Roadblocks to Cardiac Cell Therapy Using Tissue Engineering. *Journal of the American College of Cardiology* **2017**, *70* (6), 766–775. https://doi.org/10.1016/j.jacc.2017.06.012.

(54) Litviňuková, M.; Talavera-López, C.; Maatz, H.; Reichart, D.; Worth, C. L.; Lindberg, E. L.; Kanda, M.; Polanski, K.; Heinig, M.; Lee, M.; Nadelmann, E. R.; Roberts, K.; Tuck, L.; Fasouli, E. S.; DeLaughter, D. M.; McDonough, B.; Wakimoto, H.; Gorham, J. M.; Samari, S.; Mahbubani, K. T.; Saeb-Parsy, K.; Patone, G.; Boyle, J. J.; Zhang, H.; Zhang, H.; Viveiros, A.; Oudit, G. Y.; Bayraktar, O. A.; Seidman, J. G.; Seidman, C. E.; Noseda, M.; Hubner, N.; Teichmann, S. A. Cells of the Adult Human Heart. *Nature* **2020**.

(55) Buikema, J. W.; Lee, S.; Goodyer, W. R.; Maas, R. G.; Chirikian, O.; Li, G.; Miao, Y.; Paige, S. L.; Lee, D.; Wu, H.; Paik, D. T.; Rhee, S.; Tian, L.; Galdos, F. X.; Puluca, N.; Beyersdorf, B.; Hu, J.; Beck, A.; Venkamatran, S.; Swami, S.; Wijnker, P.; Schuldt, M.; Dorsch, L. M.; van Mil, A.; Red-Horse, K.; Wu, J. C. J. Y.; Geisen, C.; Hesse, M.; Serpooshan, V.; Jovinge, S.; Fleischmann, B. K.; Doevendans, P. A.; van der Velden, J.; Garcia, K. C.; Wu, J. C. J. Y.; Sluijter, J. P. G.; Wu, S. M. Wnt Activation and Reduced Cell-Cell Contact Synergistically Induce Massive Expansion of Functional Human iPSC-Derived Cardiomyocytes. *Cell Stem Cell* **2020**, *27* (1), 50-63.e5.

(56) Mills, R. J.; Parker, B. L.; Quaife-Ryan, G. A.; Voges, H. K.; Needham, E. J.; Bornot, A.; Ding, M.; Andersson, H.; Polla, M.; Elliott, D. A.; Drowley, L.; Clausen, M.; Plowright, A. T.; Barrett, I. P.; Wang, Q. D.; James, D. E.; Porrello, E. R.; Hudson, J. E. Drug Screening in Human PSC-Cardiac Organoids Identifies Pro-Proliferative Compounds Acting via the Mevalonate Pathway. *Cell Stem Cell* **2019**, *24* (6), 895-907.e6. https://doi.org/10.1016/J.STEM.2019.03.009.

(57) Sharma, A.; Zhang, Y.; Buikema, J. W.; Serpooshan, V.; Chirikian, O.; Kosaric, N.; Churko, J. M.; Dzilic, E.; Shieh, A.; Burridge, P. W.; Wu, J. C.; Wu, S. M. Stage-Specific Effects of Bioactive Lipids on Human iPSC Cardiac Differentiation and Cardiomyocyte Proliferation. *Scientific Reports 2018 8:1* **2018**, *8* (1), 1–10. https://doi.org/10.1038/s41598-018-24954-3.

(58) Chen, V. C.; Couture, S. M.; Ye, J.; Lin, Z.; Hua, G.; Huang, H. I. P.; Wu, J.; Hsu, D.; Carpenter, M. K.; Couture, L. A. Scalable GMP Compliant Suspension Culture System for Human ES Cells. *Stem Cell Research* **2012**, *8* (3), 388–402. https://doi.org/10.1016/j.scr.2012.02.001.

(59) Niebruegge, S.; Nehring, A.; Bär, H.; Schroeder, M.; Zweigerdt, R.; Lehmann, J. Cardiomyocyte Production in Mass Suspension Culture: Embryonic Stem Cells as a Source for Great Amounts of Functional Cardiomyocytes. *https://home.liebertpub.com/tea* **2008**, *14* (10), 1591–1601. https://doi.org/10.1089/TEN.TEA.2007.0247.

(60) Kempf, H.; Kropp, C.; Olmer, R.; Martin, U.; Zweigerdt, R. Cardiac Differentiation of Human Pluripotent Stem Cells in Scalable Suspension Culture. *Nature Protocols* **2015**, *10* (9), 1345–1361. https://doi.org/10.1038/nprot.2015.089.

(61) Zhang, Y. S.; Yue, K.; Aleman, J.; Mollazadeh-Moghaddam, K.; Bakht, S. M.; Yang, J.; Jia, W.; Dell'Erba, V.; Assawes, P.; Shin, S. R.; Dokmeci, M. R.; Oklu, R.; Khademhosseini, A. 3D Bioprinting for Tissue and Organ Fabrication. *Annals of Biomedical Engineering* **2017**, *45* (1), 148–163. https://doi.org/10.1007/s10439-016-1612-8.

(62) Lee, A.; Hudson, A. R.; Shiwarski, D. J.; Tashman, J. W.; Hinton, T. J.; Yerneni, S.; Bliley, J. M.; Campbell, P. G.; Feinberg, A. W. 3D Bioprinting of Collagen to Rebuild Components of the Human Heart. *Science* **2019**, *365* (6452), 482–487. https://doi.org/10.1126/science.aav9051.
(63) Noor, N.; Shapira, A.; Edri, R.; Gal, I.; Wertheim, L.; Dvir, T. 3D Printing of Personalized Thick and Perfusable Cardiac Patches and Hearts. *Advanced Science* **2019**, *6* (11). https://doi.org/10.1002/advs.201900344.
(64) Hoffman, T.; Khademhosseini, A.; Langer, R. Chasing the Paradigm: Clinical Translation of 25 Years of Tissue Engineering. *https://home.liebertpub.com/tea* **2019**, *25* (9–10), 679–687. https://doi.org/10.1089/TEN.TEA.2019.0032.
(65) Khademhosseini, A.; Langer, R. A Decade of Progress in Tissue Engineering. *Nature Protocols* **2016**, *11* (10), 1775–1781. https://doi.org/10.1038/nprot.2016.123.
(66) Ghovvati, M.; Kharaziha, M.; Ardehali, R.; Annabi, N. Recent Advances in Designing Electroconductive Biomaterials for Cardiac Tissue Engineering. *Adv Healthcare Materials* **2022**, *11* (13), 2200055. https://doi.org/10.1002/adhm.202200055.
(67) Hsiao, C.-W.; Bai, M.-Y.; Chang, Y.; Chung, M.-F.; Lee, T.-Y.; Wu, C.-T.; Maiti, B.; Liao, Z.-X.; Li, R.-K.; Sung, H.-W. Electrical Coupling of Isolated Cardiomyocyte Clusters Grown on Aligned Conductive Nanofibrous Meshes for Their Synchronized Beating. *Biomaterials* **2013**, *34* (4), 1063–1072. https://doi.org/10.1016/j.biomaterials.2012.10.065.
(68) Mihic, A.; Cui, Z.; Wu, J.; Vlacic, G.; Miyagi, Y.; Li, S.-H.; Lu, S.; Sung, H.-W.; Weisel, R. D.; Li, R.-K. A Conductive Polymer Hydrogel Supports Cell Electrical Signaling and Improves Cardiac Function After Implantation into Myocardial Infarct. *Circulation* **2015**, *132* (8), 772–784. https://doi.org/10.1161/CIRCULATIONAHA.114.014937.
(69) Gelmi, A.; Cieslar-Pobuda, A.; de Muinck, E.; Los, M.; Rafat, M.; Jager, E. W. H. Direct Mechanical Stimulation of Stem Cells: A Beating Electromechanically Active Scaffold for Cardiac Tissue Engineering. *Adv Healthcare Materials* **2016**, *5* (12), 1471–1480. https://doi.org/10.1002/adhm.201600307.
(70) Tsui, J. H.; Ostrovsky-Snider, N. A.; Yama, D. M. P.; Donohue, J. D.; Choi, J. S.; Chavanachat, R.; Larson, J. D.; Murphy, A. R.; Kim, D.-H. Conductive Silk–Polypyrrole Composite Scaffolds with Bioinspired Nanotopographic Cues for Cardiac Tissue Engineering. *J. Mater. Chem. B* **2018**, *6* (44), 7185–7196. https://doi.org/10.1039/C8TB01116H.
(71) Roshanbinfar, K.; Vogt, L.; Ruther, F.; Roether, J. A.; Boccaccini, A. R.; Engel, F. B. Nanofibrous Composite with Tailorable Electrical and Mechanical Properties for Cardiac Tissue Engineering. *Adv. Funct. Mater.* **2020**, *30* (7), 1908612. https://doi.org/10.1002/adfm.201908612.
(72) Solazzo, M.; O'Brien, F. J.; Nicolosi, V.; Monaghan, M. G. The Rationale and Emergence of Electroconductive Biomaterial Scaffolds in Cardiac Tissue Engineering. *APL Bioengineering* **2019**, *3* (4), 041501. https://doi.org/10.1063/1.5116579.
(73) Mantione, D.; Del Agua, I.; Sanchez-Sanchez, A.; Mecerreyes, D. Poly(3,4-Ethylenedioxythiophene) (PEDOT) Derivatives: Innovative Conductive Polymers for Bioelectronics. *Polymers* **2017**, *9* (12), 354. https://doi.org/10.3390/polym9080354.
(74) Keate, R. L.; Tropp, J.; Serna, C.; Rivnay, J. A Collagen-Conducting Polymer Composite with Enhanced Chondrogenic Potential. *Cel. Mol. Bioeng.* **2021**, *14* (5), 501–512. https://doi.org/10.1007/s12195-021-00702-y.

(75) Solazzo, M.; Krukiewicz, K.; Zhussupbekova, A.; Fleischer, K.; Biggs, M. J.; Monaghan, M. G. PEDOT:PSS Interfaces Stabilised Using a PEGylated Crosslinker Yield Improved Conductivity and Biocompatibility. *J. Mater. Chem. B* **2019**, *7* (31), 4811–4820. https://doi.org/10.1039/C9TB01028A.
(76) Abedi, A.; Hasanzadeh, M.; Tayebi, L. Conductive Nanofibrous Chitosan/PEDOT:PSS Tissue Engineering Scaffolds. *Materials Chemistry and Physics* **2019**, *237*, 121882. https://doi.org/10.1016/j.matchemphys.2019.121882.
(77) Kaushik, G.; Fuhrmann, A.; Cammarato, A.; Engler, A. J. In Situ Mechanical Analysis of Myofibrillar Perturbation and Aging on Soft, Bilayered Drosophila Myocardium. *Biophysical Journal* **2011**, *101* (11), 2629–2637. https://doi.org/10.1016/j.bpj.2011.10.042.
(78) Reeves, G. K.; Harrison, H. B. Obtaining the Specific Contact Resistance from Transmission Line Model Measurements. *IEEE Electron Device Lett.* **1982**, *3* (5), 111–113. https://doi.org/10.1109/EDL.1982.25502.
(79) Berger, H. H. Contact Resistance and Contact Resistivity. *J. Electrochem. Soc.* **1972**, *119* (4), 507. https://doi.org/10.1149/1.2404240.
(80) Lian, X.; Zhang, J.; Azarin, S. M.; Zhu, K.; Hazeltine, L. B.; Bao, X.; Hsiao, C.; Kamp, T. J.; Palecek, S. P. Directed Cardiomyocyte Differentiation from Human Pluripotent Stem Cells by Modulating Wnt/β-Catenin Signaling under Fully Defined Conditions. *Nat Protoc* **2013**, *8* (1), 162–175. https://doi.org/10.1038/nprot.2012.150.
(81) Andrews, Simon. FastQC: A Quality Control Tool for High Throughput Sequence Data. https://www.bioinformatics.babraham.ac.uk/projects/fastqc/.
(82) Dobin, A.; Davis, C. A.; Schlesinger, F.; Drenkow, J.; Zaleski, C.; Jha, S.; Batut, P.; Chaisson, M.; Gingeras, T. R. STAR: Ultrafast Universal RNA-Seq Aligner. *Bioinformatics* **2013**, *29* (1), 15–21. https://doi.org/10.1093/bioinformatics/bts635.
(83) Liao, Y.; Smyth, G. K.; Shi, W. featureCounts: An Efficient General Purpose Program for Assigning Sequence Reads to Genomic Features. *Bioinformatics* **2014**, *30* (7), 923–930. https://doi.org/10.1093/bioinformatics/btt656.
(84) Love, M. I.; Huber, W.; Anders, S. Moderated Estimation of Fold Change and Dispersion for RNA-Seq Data with DESeq2. *Genome Biol* **2014**, *15* (12), 550. https://doi.org/10.1186/s13059-014-0550-8.
(85) Blighe, K. EnhancedVolcano: Publication-Ready Volcano Plots with Enhanced Colouring and Labeling, 2022. https://doi.org/10.18129/B9.BIOC.ENHANCEDVOLCANO.
(86) Kassambara, Alboukadel. Ggpubr: "ggplot2" Based Publication Ready Plots, 2022. https://rpkgs.datanovia.com/ggpubr/.
(87) Raudvere, U.; Kolberg, L.; Kuzmin, I.; Arak, T.; Adler, P.; Peterson, H.; Vilo, J. G:Profiler: A Web Server for Functional Enrichment Analysis and Conversions of Gene Lists (2019 Update). *Nucleic Acids Research* **2019**, *47* (W1), W191–W198. https://doi.org/10.1093/nar/gkz369.
(88) Robinson, M. D.; McCarthy, D. J.; Smyth, G. K. edgeR: A Bioconductor Package for Differential Expression Analysis of Digital Gene Expression Data. *Bioinformatics* **2010**, *26* (1), 139–140. https://doi.org/10.1093/bioinformatics/btp616.
(89) Leek, J. T.; Johnson, W. E.; Parker, H. S.; Jaffe, A. E.; Storey, J. D. The Sva Package for Removing Batch Effects and Other Unwanted Variation in High-Throughput Experiments. *Bioinformatics* **2012**, *28* (6), 882–883. https://doi.org/10.1093/bioinformatics/bts034.

(90) Wickham, H. *Ggplot2: Elegant Graphics for Data Analysis*, 2nd ed. 2016.; Use R!; Springer International Publishing : Imprint: Springer: Cham, 2016. https://doi.org/10.1007/978-3-319-24277-4.
(91) Kolde, Raivo. Pheatmap: Pretty Heatmaps, 2019. https://CRAN.R-project.org/package=pheatmap.
(92) Salick, M. R.; Napiwocki, B. N.; Kruepke, R. A.; Knight, G. T.; Ashton, R. S.; Crone, W. C. The Scanning Gradient Fourier Transform (SGFT) Method for Assessing Sarcomere Organization and Alignment. *Journal of Applied Physics* **2020**, *127* (19), 194701. https://doi.org/10.1063/1.5129347.
(93) Doyle, A. D.; Carvajal, N.; Jin, A.; Matsumoto, K.; Yamada, K. M. Local 3D Matrix Microenvironment Regulates Cell Migration through Spatiotemporal Dynamics of Contractility-Dependent Adhesions. *Nat Commun* **2015**, *6* (1), 8720. https://doi.org/10.1038/ncomms9720.
(94) Engler, A. J.; Sen, S.; Sweeney, H. L.; Discher, D. E. Matrix Elasticity Directs Stem Cell Lineage Specification. *Cell* **2006**, *126* (4), 677–689. https://doi.org/10.1016/j.cell.2006.06.044.
(95) Engler, A. J.; Carag-Krieger, C.; Johnson, C. P.; Raab, M.; Tang, H.-Y.; Speicher, D. W.; Sanger, J. W.; Sanger, J. M.; Discher, D. E. Embryonic Cardiomyocytes Beat Best on a Matrix with Heart-like Elasticity: Scar-like Rigidity Inhibits Beating. *Journal of Cell Science* **2008**, *121* (22), 3794–3802. https://doi.org/10.1242/jcs.029678.
(96) Berry, M. F.; Engler, A. J.; Woo, Y. J.; Pirolli, T. J.; Bish, L. T.; Jayasankar, V.; Morine, K. J.; Gardner, T. J.; Discher, D. E.; Sweeney, H. L. Mesenchymal Stem Cell Injection after Myocardial Infarction Improves Myocardial Compliance. *American Journal of Physiology-Heart and Circulatory Physiology* **2006**, *290* (6), H2196–H2203. https://doi.org/10.1152/ajpheart.01017.2005.
(97) Miccoli, I.; Edler, F.; Pfnür, H.; Tegenkamp, C. The 100th Anniversary of the Four-Point Probe Technique: The Role of Probe Geometries in Isotropic and Anisotropic Systems. *J. Phys.: Condens. Matter* **2015**, *27* (22), 223201. https://doi.org/10.1088/0953-8984/27/22/223201.
(98) Kotwal, A. Electrical Stimulation Alters Protein Adsorption and Nerve Cell Interactions with Electrically Conducting Biomaterials. *Biomaterials* **2001**, *22* (10), 1055–1064. https://doi.org/10.1016/S0142-9612(00)00344-6.
(99) Garrudo, F. F. F.; Filippone, G.; Resina, L.; Silva, J. C.; Barbosa, F.; Ferreira, L. F. V.; Esteves, T.; Marques, A. C.; Morgado, J.; Ferreira, F. C. Production of Blended Poly(Acrylonitrile): Poly(Ethylenedioxythiophene):Poly(Styrene Sulfonate) Electrospun Fibers for Neural Applications. *Polymers* **2023**, *15* (13), 2760. https://doi.org/10.3390/polym15132760.
(100) Marzocchi, M.; Gualandi, I.; Calienni, M.; Zironi, I.; Scavetta, E.; Castellani, G.; Fraboni, B. Physical and Electrochemical Properties of PEDOT:PSS as a Tool for Controlling Cell Growth. *ACS Appl. Mater. Interfaces* **2015**, *7* (32), 17993–18003. https://doi.org/10.1021/acsami.5b04768.
(101) Karbassi, E.; Fenix, A.; Marchiano, S.; Muraoka, N.; Nakamura, K.; Yang, X.; Murry, C. E. Cardiomyocyte Maturation: Advances in Knowledge and Implications for Regenerative Medicine. *Nat Rev Cardiol* **2020**, *17* (6), 341–359. https://doi.org/10.1038/s41569-019-0331-x.

(102) Zhang, S.; Londhe, P.; Zhang, M.; Davie, J. K. Transcriptional Analysis of the Titin Cap Gene. *Mol Genet Genomics* **2011**, *285* (3), 261–272. https://doi.org/10.1007/s00438-011-0603-6.
(103) Zhang, J.; Liang, Y.; Bradford, W. H.; Sheikh, F. Desmosomes: Emerging Pathways and Non-Canonical Functions in Cardiac Arrhythmias and Disease. *Biophys Rev* **2021**, *13* (5), 697–706. https://doi.org/10.1007/s12551-021-00829-2.
(104) Kam, C. Y.; Dubash, A. D.; Magistrati, E.; Polo, S.; Satchell, K. J. F.; Sheikh, F.; Lampe, P. D.; Green, K. J. Desmoplakin Maintains Gap Junctions by Inhibiting Ras/MAPK and Lysosomal Degradation of Connexin-43. *Journal of Cell Biology* **2018**, *217* (9), 3219–3235. https://doi.org/10.1083/jcb.201710161.
(105) Lundy, S. D.; Zhu, W.-Z.; Regnier, M.; Laflamme, M. A. Structural and Functional Maturation of Cardiomyocytes Derived from Human Pluripotent Stem Cells. *Stem Cells and Development* **2013**, *22* (14), 1991–2002. https://doi.org/10.1089/scd.2012.0490.
(106) Lou, Q.; Janardhan, A.; Efimov, I. R. Remodeling of Calcium Handling in Human Heart Failure. In *Calcium Signaling*; Islam, Md. S., Ed.; Advances in Experimental Medicine and Biology; Springer Netherlands: Dordrecht, 2012; Vol. 740, pp 1145–1174. https://doi.org/10.1007/978-94-007-2888-2_52.
(107) Eisner, D. A.; Caldwell, J. L.; Kistamás, K.; Trafford, A. W. Calcium and Excitation-Contraction Coupling in the Heart. *Circ Res* **2017**, *121* (2), 181–195. https://doi.org/10.1161/CIRCRESAHA.117.310230.
(108) Toyofuku, T.; Yabuki, M.; Otsu, K.; Kuzuya, T.; Hori, M.; Tada, M. Intercellular Calcium Signaling via Gap Junction in Connexin-43-Transfected Cells. *Journal of Biological Chemistry* **1998**, *273* (3), 1519–1528. https://doi.org/10.1074/jbc.273.3.1519.
(109) Guatimosim, S.; Guatimosim, C.; Song, L.-S. Imaging Calcium Sparks in Cardiac Myocytes. In *Light Microscopy*; Chiarini-Garcia, H., Melo, R. C. N., Eds.; Methods in Molecular Biology; Humana Press: Totowa, NJ, 2011; Vol. 689, pp 205–214. https://doi.org/10.1007/978-1-60761-950-5_12.
(110) Priest, B. T.; McDermott, J. S. Cardiac Ion Channels. *Channels* **2015**, *9* (6), 352–359. https://doi.org/10.1080/19336950.2015.1076597.
(111) Du, D. T. M.; Hellen, N.; Kane, C.; Terracciano, C. M. N. Action Potential Morphology of Human Induced Pluripotent Stem Cell-Derived Cardiomyocytes Does Not Predict Cardiac Chamber Specificity and Is Dependent on Cell Density. *Biophysical Journal* **2015**, *108* (1), 1–4. https://doi.org/10.1016/j.bpj.2014.11.008.
(112) Roshanbinfar, K.; Vogt, L.; Greber, B.; Diecke, S.; Boccaccini, A. R.; Scheibel, T.; Engel, F. B. Electroconductive Biohybrid Hydrogel for Enhanced Maturation and Beating Properties of Engineered Cardiac Tissues. *Adv. Funct. Mater.* **2018**, *28* (42), 1803951. https://doi.org/10.1002/adfm.201803951.
(113) Martin, S. S.; Aday, A. W.; Almarzooq, Z. I.; Anderson, C. A. M.; Arora, P.; Avery, C. L.; Baker-Smith, C. M.; Barone Gibbs, B.; Beaton, A. Z.; Boehme, A. K.; Commodore-Mensah, Y.; Currie, M. E.; Elkind, M. S. V.; Evenson, K. R.; Generoso, G.; Heard, D. G.; Hiremath, S.; Johansen, M. C.; Kalani, R.; Kazi, D. S.; Ko, D.; Liu, J.; Magnani, J. W.; Michos, E. D.; Mussolino, M. E.; Navaneethan, S. D.; Parikh, N. I.; Perman, S. M.; Poudel, R.; Rezk-Hanna, M.; Roth, G. A.; Shah, N. S.; St-Onge, M.-P.; Thacker, E. L.; Tsao, C. W.; Urbut, S. M.; Van Spall, H. G. C.; Voeks, J. H.; Wang, N.-Y.; Wong, N. D.; Wong, S. S.; Yaffe, K.; Palaniappan, L. P.; on behalf of the American Heart Association Council on Epidemiology and Prevention Statistics Committee and Stroke Statistics

Subcommittee. 2024 Heart Disease and Stroke Statistics: A Report of US and Global Data From the American Heart Association. *Circulation* **2024**, *149* (8). https://doi.org/10.1161/CIR.0000000000001209.
(114) Abdelsayed, M.; Kort, E. J.; Jovinge, S.; Mercola, M. Repurposing Drugs to Treat Cardiovascular Disease in the Era of Precision Medicine. *Nat Rev Cardiol* **2022**, *19* (11), 751–764. https://doi.org/10.1038/s41569-022-00717-6.
(115) Alkalbani, M.; Psotka, M. A. Rethinking Heart Failure Clinical Trials: The Heart Failure Collaboratory. *Front. Cardiovasc. Med.* **2024**, *11*, 1350569. https://doi.org/10.3389/fcvm.2024.1350569.
(116) Lian, X.; Hsiao, C.; Wilson, G.; Zhu, K.; Hazeltine, L. B.; Azarin, S. M.; Raval, K. K.; Zhang, J.; Kamp, T. J.; Palecek, S. P. Robust Cardiomyocyte Differentiation from Human Pluripotent Stem Cells via Temporal Modulation of Canonical Wnt Signaling. *Proc. Natl. Acad. Sci. U.S.A.* **2012**, *109* (27). https://doi.org/10.1073/pnas.1200250109.
(117) Cho, S.; Discher, D. E.; Leong, K. W.; Vunjak-Novakovic, G.; Wu, J. C. Challenges and Opportunities for the next Generation of Cardiovascular Tissue Engineering. *Nat Methods* **2022**, *19* (9), 1064–1071. https://doi.org/10.1038/s41592-022-01591-3.
(118) Kim, H.; Kamm, R. D.; Vunjak-Novakovic, G.; Wu, J. C. Progress in Multicellular Human Cardiac Organoids for Clinical Applications. *Cell Stem Cell* **2022**, *29* (4), 503–514. https://doi.org/10.1016/j.stem.2022.03.012.
(119) Ergir, E.; Oliver-De La Cruz, J.; Fernandes, S.; Cassani, M.; Niro, F.; Pereira-Sousa, D.; Vrbský, J.; Vinarský, V.; Perestrelo, A. R.; Debellis, D.; Vadovičová, N.; Uldrijan, S.; Cavalieri, F.; Pagliari, S.; Redl, H.; Ertl, P.; Forte, G. Generation and Maturation of Human iPSC-Derived 3D Organotypic Cardiac Microtissues in Long-Term Culture. *Sci Rep* **2022**, *12* (1), 17409. https://doi.org/10.1038/s41598-022-22225-w.
(120) Gonzalez, G.; Nelson, A. C.; Holman, A. R.; Whitehead, A. J.; LaMontagne, E.; Lian, R.; Vatsyayan, R.; Dayeh, S. A.; Engler, A. J. Conductive Electrospun Polymer Improves Stem Cell-Derived Cardiomyocyte Function and Maturation. *Biomaterials* **2023**, *302*, 122363. https://doi.org/10.1016/j.biomaterials.2023.122363.
(121) Ronaldson-Bouchard, K.; Yeager, K.; Teles, D.; Chen, T.; Ma, S.; Song, L.; Morikawa, K.; Wobma, H. M.; Vasciaveo, A.; Ruiz, E. C.; Yazawa, M.; Vunjak-Novakovic, G. Engineering of Human Cardiac Muscle Electromechanically Matured to an Adult-like Phenotype. *Nat Protoc* **2019**, *14* (10), 2781–2817. https://doi.org/10.1038/s41596-019-0189-8.
(122) Davidson, M. D.; Prendergast, M. E.; Ban, E.; Xu, K. L.; Mickel, G.; Mensah, P.; Dhand, A.; Janmey, P. A.; Shenoy, V. B.; Burdick, J. A. Programmable and Contractile Materials through Cell Encapsulation in Fibrous Hydrogel Assemblies. *Sci. Adv.* **2021**, *7* (46), eabi8157. https://doi.org/10.1126/sciadv.abi8157.
(123) Garzoni, L. R.; Rossi, M. I. D.; De Barros, A. P. D. N.; Guarani, V.; Keramidas, M.; Balottin, L. B. L.; Adesse, D.; Takiya, C. M.; Manso, P. P.; Otazú, I. B.; Meirelles, M. D. N.; Borojevic, R. Dissecting Coronary Angiogenesis: 3D Co-Culture of Cardiomyocytes with Endothelial or Mesenchymal Cells. *Experimental Cell Research* **2009**, *315* (19), 3406–3418. https://doi.org/10.1016/j.yexcr.2009.09.016.
(124) Li, Y.; Merkel, C. D.; Zeng, X.; Heier, J. A.; Cantrell, P. S.; Sun, M.; Stolz, D. B.; Watkins, S. C.; Yates, N. A.; Kwiatkowski, A. V. The N-Cadherin Interactome in Primary Cardiomyocytes as Defined Using Quantitative Proximity Proteomics. *Journal of Cell Science* **2019**, *132* (3), jcs221606. https://doi.org/10.1242/jcs.221606.

(125) Xu, H.; Van Remmen, H. The SarcoEndoplasmic Reticulum Calcium ATPase (SERCA) Pump: A Potential Target for Intervention in Aging and Skeletal Muscle Pathologies. *Skeletal Muscle* **2021**, *11* (1), 25. https://doi.org/10.1186/s13395-021-00280-7.